Dalton Transactions

PERSPECTIVE

View Article Online
View Journal

Cite this: DOI: 10.1039/d6dt00272b

Thermoelectric metal chalcogenides: a platform for anion mixing studies

Oleksandr Dobrozhan,†[a,b] Sajida Kousar,†[a] Girish C. Tewari[a] and Maarit Karppinen*[a]

Received 2nd February 2026,
Accepted 1st April 2026

DOI: 10.1039/d6dt00272b

rsc.li/dalton

Metal chalcogenides represent state-of-the-art thermoelectric (TE) materials, both in practical TE energy conversion devices and in new TE material research. To further push the performance boundaries of these materials, the major challenge is to suppress the thermal conductivity as much as possible while maintaining high electrical transport properties. The strategies employed to address this challenge include band engineering, chemical composition tuning, and nano- and microstructural modification. Regarding chemical composition tuning, an effective approach specific to metal chalcogenide thermoelectrics is anion mixing through solid solution formation at a chalcogen site, where sulfur, selenium, and tellurium atoms can occupy the same crystallographic site. This perspectival review aims to provide first a wider overview of such possibilities among the metal chalcogenides in general and then highlight the recent research on three currently strongly emerging TE metal chalcogenide families: (i) different binary, ternary and quaternary copper chalcogenides, (ii) ternary cobalt antimony chalcogenides, and (iii) binary silver chalcogenides.

1. Introduction

The growing demand for renewable energy solutions has intensified research on advanced materials for efficient energy storage and conversion. One particularly promising approach is thermoelectric (TE) energy conversion, which enables the direct transformation of waste heat into electricity. This process relies on TE materials, which generate an electric voltage when subjected to a temperature gradient. The efficiency of TE conversion depends on multiple factors, including the design of the TE device and the temperature difference applied. However, the intrinsic properties of the TE material itself form a major factor. State-of-the-art TE materials include the traditional Pb- and Bi-based chalcogenides, with Sn-, In-, Cu-, Co-, and Ag-based systems emerging recently.[1–4]

In recent years, various new metal chalcogenide families have been highlighted as prominent TE material candidates. Compared to metal oxides, the higher bond covalency in metal chalcogenides is beneficial for enhancing the power factor (PF), while the heaviness of the chalcogen atoms results in lower thermal conductivity, such that overall, the TE figure-of-merit (ZT) is enhanced. Also importantly, metal chalcogenides can be doped into both n-type and p-type conductors and engineered into different kinds of structures; these are essential requirements for the fabrication of actual TE devices. Moreover, by controlling the anion composition in these materials, their structural, electrical, and thermal properties can be optimized.

Indeed, an effective approach specific to metal chalcogenide thermoelectrics is anion mixing *via* solid solution formation at the chalcogen site occupied by sulfur, selenium or tellurium, as opposed to mixed-anion frameworks where anions occupy distinct crystallographic positions. In the resultant metal chalcogenides, the cations are bonded to more than one kind of anion, inducing disorder in the lattice and suppressing thermal conductivity, while also providing a powerful tool for fine-tuning the electronic structure for improved electronic transport, thereby enhancing the ZT value. In Fig. 1, we summarize the expected benefits achieved by the anion mixing approach in the metal chalcogenides.

This perspectival review aims to provide, after a brief introduction to the basics of thermoelectrics in Section 2, first a wider overview of commonly used engineering approaches for tuning charge and heat transport in state-of-the-art metal chalcogenides (Section 3) and then highlight recent research on three currently strongly emerging TE metal chalcogenide families: different binary, ternary and quaternary copper chalcogenides (Section 4), ternary cobalt antimony chalcogenides (Section 5), and binary silver chalcogenides (Section 6). Finally, we make a brief outlook in Section 7.

---

[a] *Department of Chemistry and Materials Science, Aalto University, FI-00076 Espoo, Finland. E-mail: maarit.karppinen@aalto.fi*

[b] *Department of Electronics and Computer Technology, Sumy State University, 40007 Sumy, Ukraine*

† These authors contributed equally.

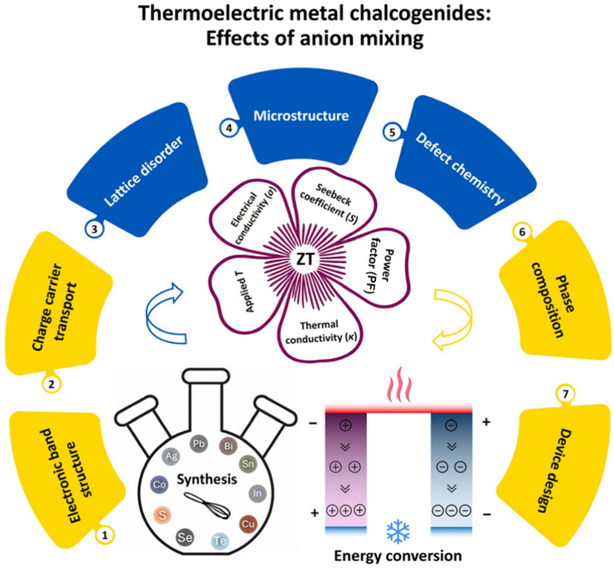

Fig. 1 Positive effects of anion mixing in metal chalcogenide thermoelectrics: (1) tailoring band gap, band alignment, and band convergence; (2.1) balancing charge carrier effective mass, concentration, and mobility; (2.2) controlling conductivity type; (2.3) suppressing bipolar effects; (3) introducing mass fluctuation and local strains; (4) designing hierarchical heterogeneity; (5) adjusting formation energies and solubility limits; (6.1) synthesizing favorable secondary phases; (6.2) stabilizing favorable phases; (6.3) tailoring polymorphic transitions; (7.1) designing new flexible and wearable device architectures; (7.2) improving device thermomechanical stability.

2. Basics of thermoelectrics

The performance of a thermoelectric material is commonly evaluated using the dimensionless figure-of-merit, $ZT = S^2\sigma T/\kappa$, where S is the Seebeck coefficient, σ is the electrical conductivity, and κ is the thermal conductivity; it is noteworthy that κ consists of both electronic (κ_e) and lattice (κ_l) contributions ($\kappa = \kappa_e + \kappa_l$). Ideally, an efficient TE material should exhibit a high Seebeck coefficient (a characteristic of semiconductors), excellent electrical conductivity (like metals), and low thermal conductivity (akin to glasses). However, optimizing these properties simultaneously is a complex task due to their interdependence.[1]

The interrelationship between electrical and thermal transport properties poses a major challenge in thermoelectric materials. Electrical conductivity depends on the charge carrier concentration (n), as expressed by: $\sigma = ne\mu$, where e is the elementary charge and μ is the carrier mobility. Meanwhile, the electronic contribution to thermal conductivity follows the Wiedemann–Franz law: $\kappa_e = L_0\ \sigma T$, where L_0 is the Lorenz number. The total thermal conductivity can then be written as: $\kappa = \kappa_l + L_0 ne\mu T$. While increasing the carrier concentration enhances electrical conductivity, it also raises thermal conductivity, thus reducing the ZT value. This trade-off highlights the difficulty of designing high-performance TE materials. To improve the ZT value, researchers typically aim to enhance the power factor (PF = $S^2\sigma$), while minimizing the lattice thermal conductivity through band structure engineering and/or nano- and microstructural modifications.[2–4]

One strategy to enhance the thermoelectric performance is to reduce the lattice thermal conductivity without negatively impacting the electrical transport properties. This has been achieved by incorporating heavy elements such as lead, thallium, bismuth, antimony, and tellurium into the TE materials, as well as designing complex crystal structures that increase phonon scattering. However, complex structures may reduce carrier mobility, thereby negatively affecting electrical conductivity.[1,5]

Thermoelectric materials have found applications in various fields, spanning from small-scale power generation to advanced aerospace and defense technologies. One of their most promising uses is in waste heat recovery, where they enhance energy efficiency by capturing excess heat from industrial processes, automotive engines, and power plants, converting it into usable electrical energy.[6–9] Similarly, wearable thermoelectric generators (TEGs) have been developed for self-powered electronics, providing sustainable energy solutions for biomedical sensors, smart textiles, and personal gadgets.[10] Thermoelectric technology is vital in aerospace and defense, providing reliable power for deep-space missions and nuclear detectors operating in extreme environments.[11,12]

An important advantage of TE modules is their solid-state operation, which makes them compact and durable.[13] Moreover, TE devices offer environmental benefits, as they operate without producing greenhouse gas emissions or relying on harmful chemicals, making them a sustainable and eco-friendly option for energy conversion. Their efficiency, reliability, and versatility continue to drive research efforts, particularly in the field of chalcogenide-based TE materials, which are being optimized for even greater performance with high mechanical and chemical stability in next-generation energy applications.

3. State-of-the-art TE metal chalcogenides

Chalcogenide materials—compounds containing sulfur, selenium, or tellurium—have emerged as key candidates for TE applications. Unlike oxides, where extensive anion substitution is thermodynamically constrained by the large mismatches in ionic size, electronegativity, and bonding character between oxygen and heavier chalcogens, chalcogenides offer far greater compositional flexibility for anion mixing, making them particularly attractive platforms for thermoelectric optimization. These materials can function as either power generators or solid-state refrigerators, depending on their operating conditions.[14] Traditionally, tellurides, such as lead telluride (PbTe) and bismuth telluride (Bi_2Te_3), have been the benchmark for TE performance due to their favorable electrical and thermal properties. However, recent research has focused on sulfur- and selenium-based compounds owing to their more abundant and less toxic constituent elements.[15–18] A key challenge with sulfides and selenides is their higher lattice thermal conductivity, which arises from their lower atomic mass (compared to the tellurides). To address this, various material tailoring approaches have been investigated.[19,20] At the same time, entirely new TE chalcogenide families are broadening the horizon; for example, significant advancements have been made in the development of environmentally friendly tin and indium chalcogenides, which show desirable semiconducting properties to properly balance charge/heat transport for efficient TE conversion. In this section, we will briefly summarize the state-of-the-art of material optimization of lead, bismuth, tin, and indium chalcogenides.

3.1. Lead chalcogenides

Lead chalcogenides (PbX; X = Te, Se, S) are among the most promising TE materials for mid-temperature applications and have been notably employed in TEGs used in NASA missions (Transit 4A, Viking 2, and Curiosity Mars rover).[15] These materials are polar semiconductors with mixed ionic-covalent bonding and a narrow bandgap (0.27–0.37 eV),[21] and their n- and p-type conductivity can be intrinsically regulated by adjusting the precise Pb/X stoichiometry.[22]

Extensive research has been devoted to optimizing the TE performance of PbTe through band convergence,[15,16] nanostructuring,[23] dislocation control,[24] doping,[25,26] and alloying.[27,28] The NaCl-type structure allows doping/alloying with compatible elements/compounds. In particular, cation doping with Mg and Se improved the *ZT* to 2.2 at 820 K,[28] with Na, Eu, and Sn to 2.5 at 900 K,[29] and with Zn and I to 1.35 at 650 K.[30]

On the other side, PbSe shows promising TE properties, outperforming PbTe at 900 K.[31] Even though intrinsic PbSe suffers from low n and high κ, these parameters can be improved by doping polycrystalline PbSe with Na (*ZT* = 1.2 at 850 K),[32] In (*ZT* = 1.6 at 850 K),[33] Cu and Te (*ZT* = 1.7 at 773 K),[34] or combining Br-doping and Cu_2Se-nanomixing (*ZT* = 1.8 at 723 K).[35] Recently, lillianite-type minerals have shown great promise as TE materials, reaching a peak *ZT* of 1.35 at 800 K for polycrystalline n-$(Pb_{0.95}Ga_{0.05})_7Bi_4Se_{13}$ samples, attributed to unusually high valley degeneracy due to alignment of nested conduction bands, strong phonon anharmonicity, and nanoscale lattice imperfection.[36]

Similar strategies have been applied to enhance the TE performance of polycrystalline PbS, which is also characterized by a low n and high κ. For example, adding CdS and ZnS nanoinclusions enhanced *ZT* up to 1.3 at 923 K,[37] Cu_2S, SrS and CaS in Na-doping – up to 1.2 at (823–923) K,[38,39] GeS and Sb-doping – up to 1.32 at 923 K,[40] (Sb, Cu) co-doping – up to 1.23 at 923 K,[41] (Sb, Cl) co-doping – up to 1.0 at 823 K,[42] and Cl-doping – up to 0.7 at 850 K.[43] Compositing is also an effective strategy for balancing electronic and thermal transport in PbS-based materials. For example, incorporating Cu or Ag can strongly increase the charge carrier concentration through spillover from metallic inclusions, while the presence of multiple phases reduces the κ_l, yielding *ZT* values of 1.1 at 750 K and 1.7 at 900 K.[44,45]

Anion mixing has been shown to be effective in enhancing the TE performance of polycrystalline Pb-based materials. For instance, anion mixing in p-type Pb(Te,Se) led to a *ZT* of 1.8 at 850 K due to high valley degeneracy, enhanced alloy scattering, and increased solubility limit for cation doping.[46] Similarly, Se substitution at the S site has been shown to be beneficial as it was found to increase bond covalency, modify effective mass, and weaken electron–phonon coupling, thereby improving charge carrier mobility. At the same time, it introduces point defects that scatter high frequency phonons. As a result, a *ZT* value of 1.7 at 900 K was achieved for $(Pb_{0.93}Sb_{0.05})(S_{0.5}Se_{0.5})$.[47] Notably, entropy-driven engineering in Na-doped $(PbTe)_{0.84}(PbSe)_{0.07}(PbS)_{0.07}$ alloys outperforms some endotaxial nanostructured counterparts due to the efficient reduction of κ_l through alloy scattering and point defects, together with simultaneous valence band modification, yielding a *ZT* of 2.0 at 800 K.[48] Moreover, the incorporation of PbSe into the ternary PbTe–PbS system broadens the solubility limit for anion doping, enabling a wider carrier concentration range. It also provides an effective means of tuning the band gap, while the strong atomic mass contrast enhances phonon scattering, resulting in an excellent *ZT* of 1.1 at 800 K for $(PbTe)_{0.75}(PbS)_{0.15}(PbSe)_{0.1}$,[49] 1.52 at 700 K for $(PbTe_{0.9295}Se_{0.07}Cl_{0.0005})_{0.93}(PbS)_{0.07}$,[50] and 1.6 at 750 K for $(Pb_{0.98}Na_{0.02})(Se_{0.1}S_{0.05}Te_{0.85})$.[51] Another notable example is $(Pb_{0.98}Na_{0.02})(Te_{0.75}Se_{0.2}S_{0.05})$, in which high-temperature band convergence and nanoprecipitations resulted in an exceptionally high *ZT* of 2.3 at 800 K.[52]

3.2. Bismuth chalcogenides

Bismuth chalcogenides (Bi_2X_3; X = Te, Se) are promising TE materials for near-room temperature applications; they are commonly utilized in TE refrigeration and power generation.[17,18] The telluride, Bi_2Te_3, is an indirect narrow bandgap (0.15 eV) material.[53–55] Due to its layered rhombohedral crystal structure, it exhibits anisotropic TE properties. The combination of highly polarized Bi–Te bonds, weak interlayer van der Waals bonding, and heavy constituent elements results in strong lattice anharmonicity and inherently low κ_l. Chalcogen modifications, *e.g.*, sintering with excess of Te, can suppress lattice and bipolar contributions to κ, reducing it to 0.38 W m^{-1} K^{-1} in p-type and to 0.48 W m^{-1} K^{-1} in n-type nanostructured Bi_2Te_3, leading to *ZT* values of 1.59 and 0.98 at 370 K, respectively.[56] Germanium doping in p-type polycrystalline Bi_2Te_3 enabled tuning of the hole concentration, yielding a *ZT* value of 0.95 at 300 K.[57]

Various doping strategies have been explored to enhance the TE efficiency of Bi_2Te_3, particularly effective being the cationic Sb-for-Bi and anionic Se-for-Te substitutions:[58] $(Bi,Sb)_2Te_3$ compositions typically exhibit p-type behavior, while $Bi_2(Te,Se)_3$ compositions favor n-type conduction.[59] Advancements in nano- and microstructural engineering have significantly improved the TE properties, with *ZT* reaching 1.86 at 373 K in p-type $(Bi,Sb)_2Te_3$ owing to enhanced phonon scattering and increased carrier mobility.[60,61] Additionally, n-type nanoplates $Bi_2(Te_{0.9}Se_{0.1})_3$ synthesized using a microwave-assisted method have demonstrated *ZT* = 1.23 at 480 K, with a remarkably reduced thermal conductivity of 0.98 W m^{-1}

K^{-1} due to grain boundary scattering, dislocations, and point defects.[62] Notably, Bi_2Te_3-based thin films have shown significantly enhanced *ZT* values compared to bulk Bi_2Te_3 alloys, with the highest values reported at 300 K of 2.75 for n-type nanoparticle-based $Bi_2(Se_{0.4}Te_{0.6})_3$ thin films and 2.4 for p-type Bi_2Te_3/Sb_2Te_3 superlattice structures.[63,64]

The Se-counterpart, Bi_2Se_3, crystallizes in a layered trigonal structure with a narrow bandgap (0.3 eV) but different electronic transport behavior in comparison with Bi_2Te_3 due to differences in defect chemistry and carrier mobility. The TE properties of Bi_2Se_3 are significantly influenced by intrinsic defects, primarily Se vacancies, which result in n-type conductivity.[65] Various cation dopants (*e.g.* Cu, In, Pb) have been explored to modulate *n* and optimize the TE performance in single crystals of $Bi_2(Se,Te)_3$.[66–68] However, Bi_2Se_3 has still remained inferior to Bi_2Te_3, due to its higher lattice thermal conductivity.

3.3. Tin chalcogenides

Tin chalcogenides (SnX; X = Se, S, Te) have sparked significant interest as TE materials due to their cation eco-friendliness, cost-effectiveness, and favorable intrinsic properties for TE conversion. The most notable member, SnSe, possesses intrinsically low κ (<0.4 W m^{-1} K^{-1} at 923 K) due to the anisotropic bonding and layered low-symmetry lattice (space group *Pnma*); this structure transforms to a high-symmetry lattice (space group *Cmcm*) at 750–800 K.[69] Exceptionally high *ZT* values have been recorded for SnSe single crystals of the *Cmcm* lattice at 923 K: 0.8 along the *a*-axis, 2.6 along the *b*-axis, and 2.3 along the *c*-axis.[69] Unfortunately, polycrystalline SnSe that is more suitable for practical applications shows a lower PF compared to single crystals due to the reduced carrier mobility.[69] For single-crystal $Sn(Se_{0.7}S_{0.3})$, S-for-Se substitution was found to shift the phase transformation to higher temperatures and enhance *ZT* at 820 K to 1.14 and 0.94 along the *b*- and *c*-axes, respectively.[70] Notably, a very low κ of 0.25 W m^{-1} K^{-1} was recorded in n-type I-doped polycrystalline SnSe,[71] and *ZT* = 2.8 at 773 K was observed for Br-doped n-type SnSe single crystals.[72]

Although SnSe has a high *ZT*, its optimization possibilities are limited by the low-temperature *Pnma* phase, which resists effective doping due to its layered structure and strongly covalent, locally distorted bonding. However, alkali metals can act as effective acceptor dopants in SnSe; *e.g.* Na-doping in single-crystal SnSe increased hole concentration by two orders of magnitude and *ZT* up to 2.0 at 773 K.[73,74] Practically high performance in p-type SnSe stems from its complex electronic band structure, while n-type SnSe achieves ultrahigh *ZT* through phonon–electron interactions and 3D-charge/2D-phonon transport.[75,76]

Due to the high cost and slow growth of single-crystal SnSe, research has shifted toward polycrystalline SnSe.[77] However, its high resistivity from low intrinsic carrier concentration makes doping essential. Alkali metal (Na, K) doping enhanced conductivity and the Seebeck coefficient *via* band convergence, achieving *ZT* = 0.8 at 800 K with just 1% doping, while Zn doping further increased *ZT* to 0.96 at 873 K.[78] Cu interstitials effectively reduced κ_l, yielding *ZT* = 1.2 at 873 K.[79] For highly textured polycrystals, *ZT* was increased to 1.05 at 873 K.[80] Textured SnSe ingots with large single-crystal domains showed suppressed κ_l, achieving a *ZT* of 1.1 at 873 K.[81]

For the sulfide, SnS, a *ZT* value of 0.16 at 823 K was reported for polycrystals.[82] In SnS single crystals, doping increased carrier concentration, boosting the *ZT* to 1.1 at 870 K with Na-doping and up to 1.6 at 873 K with Se alloying, mainly due to tailoring the electronic band structure, particularly regulating effective mass and mobility, and activating Fermi pockets.[83–85]

The telluride counterpart, SnTe, is a narrow-bandgap (0.13 eV) semiconductor; it is considered a promising, eco-friendly alternative to PbTe due to its similar band structure. However, pristine SnTe suffers from high κ_l and a large energy gap (0.35 eV at 300 K) between its light-hole (*L*) and heavy-hole (Σ) bands. Thus, achieving effective band convergence requires high dopant concentrations.[86] To address this, various doping strategies have been explored. While In, Cd and Hg showed limited solubility,[87–89] Mn proved to be more effective. Mn-doped polycrystalline SnTe exhibited enhanced *S* (80 μV K^{-1} at 300 K; 230 μV K^{-1} at 900 K), increased power factors, and a *ZT* of 1.3 at 900 K, due to band convergence and point defect scattering.[90] Alloying $AgBiTe_2$ into polycrystalline SnTe compensates the hole concentration *via* Bi electron donors and reduces thermal conductivity through point defect scattering and Ag-rich nanostructuring, yielding a *ZT* value of 1.1 at 775 K.[91]

3.4. Indium chalcogenides

Indium chalcogenides (In–X, X = Se, Te, S) represent a family of promising TE materials, with several members of In–Se adopting a two-dimensional van der Waals layered structure with weak atomic bonding, which gives rise to intrinsically low κ.[92] Common strategies for optimizing the TE performance of In–X materials include defect engineering, nanostructuring, and grain size engineering.[92]

Among them, anion mixing represents one of the most effective strategies for defect engineering and band manipulation. For instance, isoelectronic doping with S atoms at the Se site was demonstrated to suppress the annihilation of donor defects (V_{In} and In_i), yielding a peak *ZT* of 0.67 in polycrystalline α-$In_2S_{0.05}Se_{2.95}$ at 923 K.[93] Furthermore, Se substitution in polycrystalline $In_{2.67}S_4$ thiospinels enhanced the charge carrier concentration – a well-known limiting factor in In–X materials – and promoted stabilization of the thermoelectrically favorable α-phase. This was attributed to the simultaneous reduction of both the band gap and the effective electron mass. Additionally, structural disorder in the ternary thiospinel contributed to a reduction in κ. Collectively, these effects resulted in an approximately 2.5-fold improvement in *ZT*, reaching a maximum of 0.25 at 760 K in $In_{2.67}S_{3.5}Se_{0.5}$.[94]

Besides that, anion substitution of Se by Te in polycrystalline $In_{0.96}Bi_{0.04}Se_{0.97}Te_{0.03}$ introduced effective phonon scattering centers, thereby reducing the κ_l. The synergistic effect of cation–anion co-doping in this system yielded a maximum *ZT* of 0.13 at 630 K.[95] Moreover, Te substitution can also improve the PF through an increase in the effective mass; as a result, *ZT* was enhanced more than twofold, reaching 0.096 at 700 K in $In_{0.9}Si_{0.1}Se_{0.93}Te_{0.07}$.[96] Anion substitution with 7% S or Te in polycrystalline InSe alloys effectively increased σ with a more pronounced effect observed for Te-doped samples owing to their smaller band gap. Both dopants also reduced κ *via* point defect phonon scattering. Consequently, *ZT* reaches maxima of 0.13 and 0.28 at 735 K for $InSe_{0.93}S_{0.07}$ and $InSe_{0.93}Te_{0.07}$.[97]

4. Copper chalcogenides

The abundance of copper in nature and the promising TE characteristics of some Cu-based compounds have been the reasons for the research efforts towards Cu-based TE applications. Initial interest in Cu_2S as a TE material dates back to the 19th century.[98] However, the first Cu-based TE devices showed operational instability due to Cu^+ ion migration.[99] More recently, suppressing ion migration has renewed interest in Cu-based thermoelectrics, with doping, structural modification, and nanostructuring widely explored to improve stability and TE performance.[100–103]

Binary Cu_2X and ternary $CuCrX_2$ chalcogenides containing monovalent copper have been widely investigated because of their high ionic conductivity and ultralow κ_l, arising from the liquid-like behavior of Cu^+ ions. Structurally, binary Cu_2X compounds comprise a rigid X-atom framework responsible for electronic transport and a disordered, mobile Cu^+ sublattice that suppresses transverse and shear vibrations, thereby reducing κ_l.[104–107] Indeed, binary Cu_2X (X = S, Se, Te) chalcogenides exhibit phase transitions and ultralow lattice thermal conductivity ($<0.8\ W\ m^{-1}\ K^{-1}$) despite the low atomic mass of Cu. Cu_2S, for example, transforms from monoclinic γ to hexagonal β at 370 K and then to superionic cubic α at 700 K.[108] The α-phase contains an fcc S^{2-} framework and highly disordered Cu^+ ions, resulting in superionic conductivity. Cu_2S is an intrinsic semiconductor, while Cu deficiency readily induces p-type behavior. Many Cu_2S-based compositions display excellent TE properties with $ZT > 1.0$, and Cu_2S:3%Pb reaches $ZT = 2.0$ at 880 K.[109] Stability-oriented strategies, such as structural stabilization and suppression of sulfur loss and Cu segregation, also promote high TE performance and PF.[110] Alloying with Te and introducing nanoscale mosaicity in polycrystalline $Cu_2(S_{0.52}Te_{0.48})$ produced a high *ZT* of 2.1 at 1000 K, mainly due to its exceptionally low κ_l of 0.3–0.4 $W\ m^{-1}\ K^{-1}$. Mosaicity offers a distinct route for tuning TE properties by enabling efficient electron transport along quasi-single-crystalline frameworks while strongly scattering phonons at strained lattice regions and mosaic nanograin interfaces.[111]

In contrast, Cu_2Se is an intrinsically p-type conductor with a bandgap of 1.2–2.3 eV.[112] Near 400 K, α-Cu_2Se transforms to the fast ion-conducting β-phase, where an fcc Se framework and disordered Cu^+ ions give rise to liquid-like thermal conductivity (0.34–0.60 $W\ m^{-1}\ K^{-1}$) while maintaining high electrical transport.[113–119] Its TE performance has been markedly enhanced since 2012, reaching a *ZT* of 1.8 by self-propagating synthesis and melt-quenching and a *ZT* of 2.6 at 850 K for Cu_2Se:1 mol% In.[120–122] Yet, instability under strong electric fields and large temperature gradients still limits applications, although operation below a critical voltage and Cu excess can improve stability.[123,124] By employing a melt-solidification technique, Zhao *et al.*[125] improved *ZT* up to 1.9 at 973 K in polycrystalline samples, though stability issues persisted due to high ion mobility. To address these challenges, $Cu_2(Se,S)$ solid solutions were developed, where anion mixing enhances structural stability. Besides the intrinsically low thermal conductivity originating from the liquid-like Cu^+ sublattice, mixed-anion solid solution formation further reduces lattice thermal conductivity *via* defect-induced phonon scattering and simultaneously optimizes carrier concentration. A *ZT* of 2.0 at 1000 K was achieved for polycrystalline $Cu_2(Se_{0.92}S_{0.08})$ with improved stability, owing to stronger bonding that fixed Cu atoms in the lattice for suppressed Cu vacancy formation and reduced the transverse sound velocity, thus leading to optimal carrier concentration and lowered thermal conductivity.[126] Similar behavior was observed by Zhao *et al.* in polycrystalline $Cu_2(Se_{0.8}S_{0.2})$, where point-defect phonon scattering in the solid solution resulted in extremely low lattice thermal conductivity (0.2–0.4 $W\ m^{-1}\ K^{-1}$) and a peak *ZT* of 1.65 at 950 K.[127] A peak *ZT* of 2.3 at 1000 K was achieved in polycrystalline $Cu_{1.94}(Se_{0.5}S_{0.5})$.[128]

The crystal structure of Cu_xTe remains debated due to the presence of closely related Cu_2Te, CuTe, and $CuTe_2$ phases at different temperatures.[129,130] However, its cubic ε-phase above 850 K exhibits promising TE performance, reaching $ZT = 0.29$ in undoped Cu_2Te and 1.0 in Ag-doped Cu_2Te at 900 K.[129] An ultralow κ_l (0.17 $W\ m^{-1}\ K^{-1}$) has been observed in $Cu_5TeS_3I_3$ polycrystals *via* coordination design for partial ionization of the Cu–I bonds, leading to reduced transverse speed of sound ($\nu_T = 839\ m\ s^{-1}$) and high anharmonicity ($\gamma = 2.76$).[131]

Similarly, ternary $CuCrX_2$ (X = S, Se) compounds exhibit κ owing to Cu^+ ion mobility.[132] They adopt a hexagonal layered structure with Cu^+ ions located at tetrahedral sites between CrX_2 layers.[133–140] In $CuCrSe_2$, Cu^+ redistribution above 365 K induces kinetic disorder, markedly lowering κ_l while maintaining high σ; a similar effect occurs in $CuCrS_2$ above 675 K.[134,135,138,141–143] $CuCrSe_2$ further shows promising transport properties and reaches $ZT = 1.0$ at 773 K.[132,138,144–146] For $CuCrS_2$, a high *ZT* value of 2.0 at RT was initially reported.[147] The subsequent attempts by Kaltzoglou *et al.*[148] to reproduce these results under analogous synthesis conditions yielded a *ZT* of only 0.023, suggesting that the originally reported value may be sensitive to differences in the microstructure or measurement methodology. Despite their promising TE properties, phase-pure $CuCrSe_2$ is difficult to synthesize by conventional methods because of secondary phases such as $CuCr_2Se_4$.[146,149] Accordingly, high-temperature treatment with water quenching, mechanical alloying followed by annealing, and spark plasma sintering (SPS) have been used to suppress impurity formation.[139,150,151] $CuCrX_2$ compounds are also highly sensitive to synthesis temperature because of native defect formation; sintering at elevated temperatures improves TE performance *via* partial Cr redistribution.[133,135–137] We further found that Se/S anion mixing in $CuCr(S,Se)_2$ drives a semiconductor-to-metal transition, narrows the bandgap, increases n, and lowers κ, all of which favor high TE performance.[152] Moreover, Se-for-S substitution changes the magnetic state from long-range antiferromagnetism to a spin-glass-like regime with gapless spin-liquid-like excitations.[153]

Beyond the Cu_2X and $CuCrX_2$ families, several other multicomponent Cu-based chalcogenides have emerged as promising TE materials. For example, BiCuSeO is a notable quaternary p-type thermoelectrics.[154] Its low κ enables high TE performance, with ZT reaching 1.1 through co-doping with (Ba, Ca, Pb)[155–157] and anion mixing with Te.[158] Moreover, argyrodite-like materials with multiple chalcogenide anions, *e.g.* bulk $Cu_8GeSe_4Te_2$,[159] have emerged as promising PLEC (phonon-liquid electron-crystal) candidates, characterized by dynamically disordered crystal structures that give rise to ultralow κ_l. Another example is polycrystalline low-symmetry $Cu_2Hf_{0.8}Ti_{0.2}Te_3$, in which electronic band nesting and hierarchical bonding formation collectively enhance the PF and suppress κ_l, yielding a ZT peak of 1.11 at 873 K.[160] Also, anion mixing in argyrodite-type copper chalcogenides is an effective strategy for stabilizing the high-symmetry cubic phase at lower temperatures through configurational entropy engineering.[161] This structural stabilization promotes a multivalley electronic structure of the valence band, modulates carrier concentration, and reduces κ_l up to 0.2–0.3 W m^{-1} K^{-1}, collectively enhancing the TE performance. Representative examples include $Cu_{8-x}GeS_{4.36}Te_{1.64}$ (ZT = 0.20 at 670 K),[162] $Cu_7P(S,Se)_6$ (ZT = 0.75 at 673 K),[163] and $Cu_8SiS_3Se_3$ (ZT = 1.24 at 773 K)[164] among others.

Antimony-containing compounds such as Cu_3SbSe_4, $CuSbSe_2$, and Cu_3SbSe_3 demonstrate the important role of Sb^{3+} lone-pair electrons in lowering κ.[165] Cu_3SbSe_4, for example, shows strongly reduced κ at elevated temperatures, and its TE performance can be enhanced to ZT = 0.7 by Sn doping.[166] Other promising Cu-based chalcogenides include $CuGaTe_2$, $CuInTe_2$, $Cu_2Zn(Sn_{0.9}In_{0.1})Se$, and $Cu_2(Sn_{0.9}In_{0.1})Se_3$, with reported ZT values approaching or exceeding unity.[167–171] Among copper sulfides, tetrahedrites, colusites, and bornite also show attractive TE performance owing to intrinsically low thermal conductivity, with the best reported ZT values of 1.0–1.2.[172–175]

Particular attention in multicomponent chalcogenides has been paid to the role of crystal structure and phase transitions in TE performance. For example, Cu_2SnSe_3 adopts a monoclinic structure with a three-dimensional hole-conducting network, which contributes to its favorable TE properties.[176] In contrast, $Cu_2ZnSn(S,Se)_4$ and $Cu_2CdSnSe_4$ possess distorted diamond-like structures, where the multielement nature suppresses phonon transport and lowers κ.[177,178] $CuInTe_2$ and $CuGaTe_2$ undergo structural phase transitions associated with cation disorder, which also affects the transport behavior.[179–181] Similarly, Cu_2ZnSnS_4 exhibits phase transitions at 530 K and 1149 K.[182,183] Overall, further enhancement of TE performance in multicomponent copper chalcogenides relies on band engineering, doping/alloying, compositing, and entropy engineering, enabling $ZT > 1$.[184,185]

In addition, copper-based systems with alkali, alkaline-earth, and rare-earth metals are also of considerable interest for TE applications.[186–191] Hodges *et al.* synthesized a series of bulk copper chalcogenides, $ACu_{4.2}TeS_2$ (A = K, Rb, Cs), in which the mixed-anion motif expands the Cu sublattice relative to ACu_4S_3, accommodating additional interstitial Cu atoms, resulting in high n (2×10^{21} cm^{-3}).[192] Jafarzadeh *et al.* synthesized polycrystalline $BaCu_{6-x}Se_{1-y}Te_{6+y}$ samples in which the Se/Te ratio adjusts Cu deficiency and thus n, with $BaCu_{5.74}(Se_{0.46}Te_{6.54})$ achieving an electrical conductivity of 685 S cm^{-1}. While increased Se/Te mass fluctuation increased material stability and reduced κ_l, the simultaneously decreased Seebeck coefficient prevented a net improvement in ZT.[193] Early reports demonstrated that substitution of S by Te reduces the band gap in LaCuSTe and SmCuSTe.[194] This finding is corroborated by recent studies on Cu_3RETe_3 (RE = Er, Ho, Tb), where the fully Te-based compositions yield promising TE performance, with peak ZT values ranging from 0.7 to 0.9 at 873 K.[195]

5. Cobalt chalcogenides

Cobalt chalcogenide thermoelectrics are currently gaining increasing interest owing to their many attractive properties such as environmental friendliness, convenient preparation, stability and promising TE characteristics. So far, the natural mineral CoSbS first identified in mineralogy in the 1970s has drawn the most attention.[196] This compound exists in two distinct structural forms, paracostibite and costibite, exhibiting different electronic properties. Both the paracostibite and costibite structures are orthorhombic, but the atomic arrangements are different (Fig. 2).

For the TE application, the paracostibite CoSbS structure is more advantageous; in this structure the Sb and S atoms form a layered arrangement within which the Co atoms occupy interstitial sites. This results in an n-type semiconductor with an indirect bandgap of 0.5 eV.[197–200] In contrast, costibite CoSbS is a semimetal with the conduction band minimum overlapping with the valence band maximum.[198,201] The key

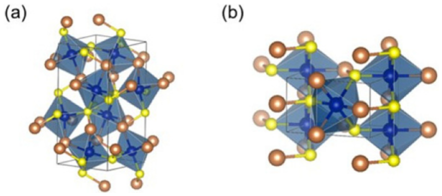

Fig. 2 Crystal structures of (a) paracostibite and (b) costibite CoSbS: Co, Sb, and S atoms are represented in blue, gold, and yellow, respectively. Paracostibite crystallizes in the space group *Pbca*, while costibite adopts the space group $Pmn2_1$. Reproduced with permission from AIP Publishing ©2020 (License CC BY).[196]

structural difference between the two lies in the degree of atomic distortion and bonding interactions; paracostibite exhibits a more distorted coordination environment that contributes to its semiconducting behavior, whereas the relatively symmetric atomic arrangement facilitates the metallic conduction of costibite. The more distorted paracostibite structure comprises 24 atoms and 8 formula units per unit cell (a = 5.843 Å, b = 5.956 Å, and c = 11.667 Å), whereas costibite has a unit cell consisting of 6 atoms and 2 formula units (a = 4.873 Å, b = 5.852 Å, and c = 3.608 Å).[196,198,200,201] Paracostibite is the high-temperature polymorph of CoSbS, and it is stable up to 1073 K.[202]

Paracostibite CoSbS was studied as a TE material for the first time in 2011 by Carlini *et al.*[203] Since then, it has gained continuous research interest owing to its flexibility for chemical substitutions, no intrinsic doping limit, high band degeneracy near the Fermi level, a high Seebeck coefficient (200 μV K^{-1}), and a large power factor (2700 μW m^{-1} K^{-2}).[196] Electronic band structure calculations revealed that CoSbS has several low-lying conduction band minima and multiple electronic pockets, which are favorable for good TE performance. Interestingly, a gigantic low-temperature (40 K) S of 2.5 mV K^{-1} was reported for a single crystal, being notably higher than the values measured for polycrystalline samples.[203–205]

Paracostibite CoSbS is readily fabricated using various synthesis techniques: ball milling,[206–208] a vapor phase technique,[203] solid-state synthesis followed by SPS for pellet densification,[201,209–211] and a heat-up method followed by two-step hot-pressing for nanoparticle synthesis.[196] Chemically synthesized nanoparticles offer advantages such as enhanced phonon scattering to reduce κ.[196,212] The thermal conductivity of CoSbS is unfortunately high (8 W m^{-1} K^{-1}) compared to state-of-the-art TE materials due to stiff bonds and light anions.

Density functional theory (DFT) calculations predicted that a high ZT value up to 1.0 at 600 K could be achieved for optimized CoSbS if the high κ can be significantly reduced.[203,213] To reduce κ and to optimize the TE performance, various cation substitutions with Ni, Te, Se, Zn, Mn, Fe, Cu, Pd, and Cr have been investigated. Partial Ni-for-Co substitution decreased the κ to 3.5 W m^{-1} K^{-1} at 600 K,[206,214] while the Cu-for-Co and Cr-for-Co substitutions reduce κ to 2–3 W m^{-1} K^{-1} (at 700–900 K), respectively.[207,215] Selenium is an efficient anionic dopant as it decreases the formation energy of point defects, suppressing κ to 3 W m^{-1} K^{-1} at 600–900 K through mass and strain fluctuations; this leads to enhanced Umklapp scattering.[211,216–218]

Similarly, Te-for-Sb substitution could reduce κ to 2.23 W m^{-1} K^{-1} due to point defect scattering, Umklapp scattering, mass fluctuation (mass difference in Sb and Te), and strain fluctuation (size difference in Sb and Te).[209,210,219] On the other hand, simultaneous introduction of Se and Ni could not decrease κ below 2.73 W m^{-1} K^{-1}.[201,208]

Recently, our group succeeded in massively suppressing κ down to 1.32 W m^{-1} K^{-1} for the $Co(Sb_{0.9}Ge_{0.1})(S_{0.95}Se_{0.05})$ composition due to softening of the low energy acoustic phonon modes and strong scattering of phonons from Ge and Se born defects.[220] DFT calculations on Ge-doped CoSbS involved replacing 12.5% of the Sb atoms with Ge. This substitution leads to a slight (2%) reduction in unit cell volume and a modest (1–4%) decrease in bond lengths. Importantly, Ge acts as an acceptor dopant by introducing metallic behavior: it shifts the Fermi level into the valence band, as shown in Fig. 3, thereby enhancing electrical conductivity.

Phonon dispersion analysis confirmed that both non-substituted and Ge-for-Sb substituted CoSbS are dynamically stable. However, Ge substitution alters the vibrational properties by lifting the degeneracy of the transverse acoustic (TA) modes and softening the TA_1 branch along the Γ–X–S–U–R path. A nearly dispersionless phonon mode also appears at around 33 meV. Projected phonon density of states (PDOS) reveals that Ge predominantly affects low-energy phonons, reducing their group velocity and enhancing phonon scattering, as shown in Fig. 4.

These computational insights explain the experimental observation that upon the Ge-for-Sb substitution, lattice thermal conductivity drops dramatically from 5.17 W m^{-1} K^{-1} to 1.32 W m^{-1} K^{-1}, approaching the theoretical minimum. Fig. 5a shows the thermal conductivity data for Ge-for-Sb and Se-for-S co-substi-

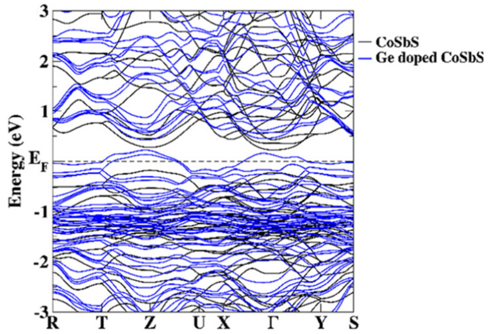

Fig. 3 Electronic band structures of CoSbS (black) and Ge-substituted $Co(Sb_{0.875}Ge_{0.125})S$ (blue). Reproduced with permission from The Royal Society of Chemistry ©2024 (License CC BY 3.0).[220]

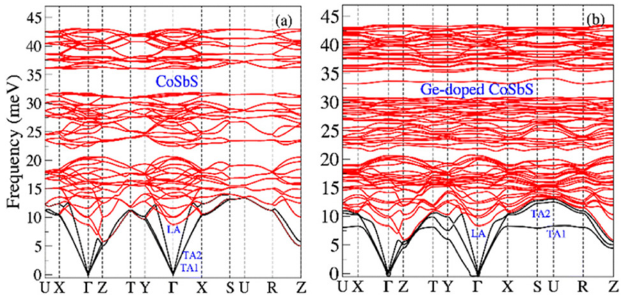

Fig. 4 DFT-calculated phonon dispersion curves for (a) CoSbS and (b) Ge-doped CoSbS ($Co(Sb_{0.875}Ge_{0.125})S$). Black lines represent the acoustic phonon modes, while red lines indicate the optical phonon modes. Reproduced with permission from The Royal Society of Chemistry ©2024 (License CC BY 3.0).[220]

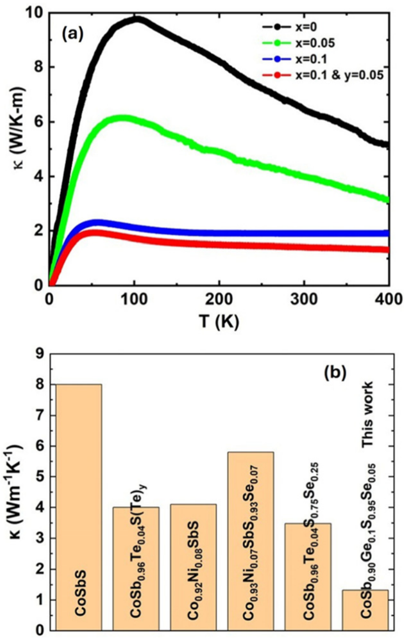

Fig. 5 (a) Temperature-dependent thermal conductivity of Co(Sb,Ge)(S,Se) samples. (b) Comparison of thermal conductivity at 400 K for CoSbS-based materials studied in this work and in previous reports. Reproduced with permission from The Royal Society of Chemistry ©2024 (License CC BY 3.0).[220]

tuted CoSbS. The reduction seen for *κ* is attributed to increased phonon–defect interactions and phonon dispersion analysis. The phonon mean free path (MFP) shortens considerably with Ge incorporation, confirming enhanced phonon scattering. Fig. 5b shows the thermal conductivity plot for different compositions of CoSbS-based materials.

CoSbS is widely reported as an n-type semiconductor in the 200–900 K temperature range.[201,205,206,209,210,214] However, it has also been reported as a p-type material with a gigantic PF below RT.[204] Upon substitutions with Ni-for-Co, Te-for-Sb, and Se-for-S, n-type conduction is observed.[201,206,209,214,221,222] In contrast, a transition in conduction from p-type to n-type is observed at 475 K when substituted with Cu-for-Co and Se-for-S.[207,216,219,223] These findings suggest the bipolar nature of CoSbS, which needs systematic study for deeper understanding.

Recently we confirmed the bipolarity of CoSbS by slightly changing the vapor pressure of sulfur during synthesis; this was shown to change the type of conductivity from p- to n-type.[224] Fig. 6 illustrates how sulfur stoichiometry influences the conduction type in CoSbS. When the material is sulfur-deficient, it exhibits p-type behavior, indicated by positive Seebeck and Hall coefficients. In contrast, sulfur-rich compositions result in n-type conduction, where both the Seebeck and Hall coefficients are negative.

Predictions based on Wiedemann–Franz law considerations and DFT calculations have suggested that *ZT* values higher than unity at high temperatures should be possible for properly optimized CoSbS.[203,205] Early experimental attempts for partially Ni-for-Co substituted samples reached *ZT* values up to 0.50 at 873 K when using ball milling to synthesize nanostructured samples.[206,214] By means of the anionic Se substitutions only, the *ZT* value could not be increased beyond 0.35.[211,216,225]

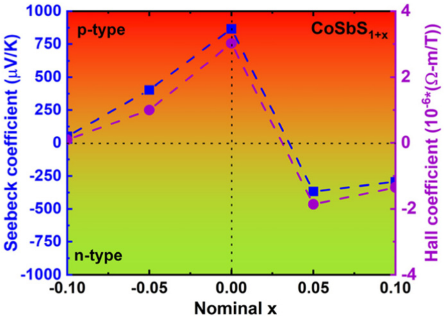

Fig. 6 The p-type to n-type conductivity transition as a function of sulfur content in CoSbS. The Seebeck coefficient (blue, left axis) and the Hall coefficient (purple, right axis) of CoSbS plotted against nominal sulfur stoichiometry. Reproduced with permission from AIP Publishing ©2022 (License CC BY 4.0).[224]

However, by combining the Se-for-S and Ni-for-Co substitutions, a record-high *ZT* value of 0.58 was realized at 900 K.[215,223] The reason behind this is that the Ni-for-Co substitution increases *n* and *m**, while the larger atomic radius of Se as compared to S softens the bonding, hence enhancing the phonon scattering. In line with this, Te-for-S substitution has been found to remarkably reduce *κ* owing to point defect scattering and also to increase *n*, leading to a jump in the PF to the highest reported value of 2.7 W m^{-1} K^{-1} and an enhanced *ZT* value to 0.47 at 725 K.[208,210] Co-substitutions with Te and Ni or Te and Se have been found effective as well, increasing the *m** and reaching the highest reported *ZT* value of 0.65 at 873 K[208] and 0.62 at 730 K.[201]

The selenium- and tellurium counterparts of CoSbS are somewhat different from the sulfur-based compound. Early reports suggest that CoSbSe exhibits an orthorhombic structure with the space group *Pnn*2. However, Chmielowski *et al.*[201] later reported that the exact space group is *Pnm*21, with a band gap of 0.4 eV. The phase shows low resistivity ($<10^{-3}$ Ω cm),[199,201,226] high carrier density (10^{21} cm^{-3}), and metallic behavior with a small negative Seebeck coefficient of −14 μV K^{-1} at RT. Despite the high carrier density, the *κ* of CoSbSe is mainly governed by lattice contributions.[227] The corresponding characteristics of CoSbTe are a pseudo-orthorhombic structure (*Pnn*2) and metallic transport behavior with a carrier density of the order of 10^{22} cm^{-3}. The RT Seebeck coefficient is negative (−7.5 μV K^{-1}) and the thermal conductivity behavior resembles that of metallic alloys, with a significant electronic contribution.[227,228] In Table 1, we summarize the early progress in optimizing the TE characteristics of various CoSb(S,Se,Te) compositions.

6. Silver chalcogenides

Flexible and wearable thermoelectric converters have attracted significant attention for their potential to contribute to sus-

Table 1 Yearly progress in optimizing the TE properties of Co-based mixed chalcogenides

Year	Composition	Synthesis	κ	ZT	T	Ref.
2024	$Co(Sb_{0.8}S_{0.8}Se_{0.4})$	SSS + SPS	2.6	0.3	823	217
2024	$Co(Sb_{0.9}Ge_{0.1})(S_{0.95}Se_{0.05})$	SSS	1.32	0.1	400	220
2023	$Co(Sb_{0.9}Se_{0.1})S$	SSS + SPS	3.02	0.22	823	218
2022	$(Ni_{0.10}Co_{0.90})Sb(S_{0.85}Se_{0.15})$	SSS	3.0	0.52	876	215
2022	$(Co_{0.94}Ni_{0.06})Sb(S_{0.96}Te_{0.04})$	BM	2.0	0.65	873	208
2020	CoSbS nanoparticles	HP	2.0	0.05	661	196
2020	$Co(Sb_{0.96}Te_{0.04})(S[Te]_{0.28})$	SSS + SPS	2.73	0.45	773	210
2019	$(Co_{0.06}Cu_{0.04})SbS$	BM	2.0	0.12	723	207
2018	$(Co_{0.93}Ni_{0.07})Sb(S_{0.93}Se_{0.07})$	SSS + SPS	2.4	0.58	900	223
2018	$Co(Sb_{0.93}Te_{0.07})S$	SSS + SPS	2.23	0.43	900	219
2017	$(Co_{0.95}Zn_{0.05})Sb(S_{0.85}Se_{0.15})$	SSS + SPS	3.8	0.34	875	225
2017	$Co(Sb_{0.96}Te_{0.04})\ (S_{0.75}Se_{0.25})$	SSS + SPS	3.48	0.62	730	201
2017	$CoSb(S_{0.85}Se_{0.15})$	SSS + SPS	4.72	0.35	923	211
2017	$CoSb(S_{0.99}Se_{0.01})$	SSS + SPS	3.0	0.26	900	216
2016	$Co(Sb_{0.96}Te_{0.04})S$	SSS + SPS	4.0	0.47	725	209
2015	$(Co_{0.92}Ni_{0.08})SbS$	BM	3.6	0.5	873	206
2013	$(Co_{0.94}Ni_{0.06})SbS$	SSS	3.5	0.35	773	214

The units for κ and T are W m^{-1} K^{-1} and K, respectively. Abbreviations for synthesis and processing: SSS = solid-state synthesis; BM = ball milling; SPS = spark plasma sintering; HP = hot pressing.

tainable development, particularly in the generation of affordable and clean energy.[229] TEGs demonstrate great promise in supplying energy to low-power electronics, thereby reducing battery dependency and minimizing electronic waste.[230] However, the inherent brittleness and low plasticity of chalcogenides limit their mechanical performance in flexible electronics.[231] Overcoming these challenges, Ag-based chalcogenides with mixed S, Se, and Te anions emerge as promising materials for flexible and wearable thermoelectric converters due to their intrinsic ductility and high TE efficiency near room temperature, while also offering the necessary mechanical properties for flexible electronics.[231–236]

Binary silver chalcogenides (Ag_2S, Ag_2Se, Ag_2Te) with n-type conductivity crystallize in multiple polymorphic forms and undergo several phase transitions upon heating.[233] At room temperature, α-Ag_2S and β-Ag_2Te adopt a monoclinic structure (space group $P2_1/c$), while β-Ag_2Se exhibits an orthorhombic structure (space group $P2_12_12_1$). Upon heating, all three compounds transition into distinct cubic crystal structures, while Ag_2S and Ag_2Te undergo at least two phase transitions. The Ag_2S semiconductor is distinguished by its remarkable ductility, attributed to the rearrangement of atoms within the unit cell without bond breaking under pressure, as confirmed by DFT simulations.[237] Ag_2S materials can withstand up to 50% compressive strain, 20% bending strain, and 4.2% tensile strain.

Meanwhile, the monoclinic Ag_2Te and orthorhombic Ag_2Se phases appear brittle at RT, in contrast to their more ductile sulfur-containing analogs. The analysis of TE transport in Ag_2S reveals that this compound, with a relatively wide band gap ($E_g \approx 1.0$ eV),[238] exhibits a near-zero ZT at RT, primarily due to its low electrical conductivity ($\sigma \approx 10$ S m^{-1}). This low σ results from the low carrier concentration ($n \approx 10^{14}$–10^{15} cm^{-3}).[233] Moreover, the high volatility of sulfur can alter the Ag-to-S stoichiometry, leading to a non-optimal concentration of interstitial Ag defects, which, in turn, significantly impacts the carrier concentration even at low concentrations.[239–242] In contrast, β-Ag_2Se and β-Ag_2Te, with E_g values of 0.05–0.20 eV,[243,244] exhibit significantly higher TE performance, reaching ZT values of 0.60–0.96 at RT, primarily due to the high carrier mobilities (μ).[245,246] Notably, $Ag_2(S,Se,Te)$ compounds exhibit low lattice thermal conductivity ($\kappa_l < 0.6$ W m^{-1} K^{-1}), attributed to structural disorder and liquid-like motion of Ag ions.[234] Thus, the development of silver-based chalcogenide materials that combine the high ductility of Ag_2S with the excellent TE properties of Ag_2Se and Ag_2Te represents a promising approach for enhancing the performance and durability of flexible TEGs. This can be achieved through anion substitution in Ag_2X *via* doping, alloying, and composite formation, all of which have been shown to enhance ZT by optimizing the n and μ through precise band structure engineering and reducing the formation energy of Ag defects. Also, anion substitution can reduce κ_l by forming multiscale phonon scattering centers. Table 2 summarizes the TE properties of the Ag-based materials with mixed chalcogens reported since 2020.

The first-principles calculations by Nam *et al.*[247] revealed that the single substitution of Ag with transition metals has little impact on the TE performance of binary Ag_2S. In addition, Wuliji *et al.*[248] examined 17 aliovalent dopants for α-Ag_2S, which shows their extremely low doping limit (<0.002%), highlighting the crucial role of lattice manipulation at the anion site. In contrast, isovalent Se and Te dopants effectively modulate both the electronic band structure and the formation energies of Ag interstitials, enabling carrier concentration adjustment by 2–3 orders of magnitude.

This was further supported by Nam *et al.*[249] and Sato *et al.*,[250] whose first-principles calculations of the electronic transport properties in the crystal structure of $Ag_2(S,Se)$ (Fig. 7a) revealed that Se alloying reduces the band gap (Fig. 7b–d), lowers the electron effective mass (m^*), and decreases the formation energy of Ag interstitials.

Table 2 Summary of the notable TE properties of Ag-based mixed chalcogenides reported since 2020

Year	Composition	ZT	T	σ	S	PF	κ	κ_l	Synthesis and processing	Ref.
2025	$(Ag_{1.99}Au_{0.01})(S_{0.5}Te_{0.5})$	0.95	550	221	−170	6.4	0.37	0.19	MeltAnneal, Cut	255
2025	$Ag_2Te–Ag_2S$	0.42	373	700	−118	9.7	0.86	0.40	SolvoS, SPS	272
2024	$(Ag_{1.9}Sn_{0.1})(S_{0.7}Se_{0.3})$	0.42	343	500	−100	5.0	0.41	0.18	MeltAnneal, Quench, Cut	253
2024	$Ag_{1.9992}(S_{0.7}Te_{0.3})$	0.85	550	329	−150	7.4	0.48	—	MeltAnneal, Cut	240
2024	$Ag_2(S_{0.7}Te_{0.3})$	0.59	723	449	−118	6.3	0.77	0.24	MeltAnneal, Quench, SPS	258
2024	$Ag_2Se–1.0\%Bi_2S_3$	0.96	370	1040	−160	26.6	1.03	0.45	HydS, HP	262
2024	$Ag_2(Te_{0.5}S_{0.5})$	1.34	523	592	−114	7.7	0.30	—	MeltAnneal, Quench, Cut	265
2024	$Ag_2(Te_{0.9}S_{0.1})$	0.60	600	402	−130	6.8	0.68	0.26	MeltAnneal, Cut	267
2024	$Ag_{1.98}(S_{0.34}Se_{0.33}Te_{0.33})$	0.85	500	236	−180	7.6	0.45	0.25	MeltAnneal, Cut	239
2024	$Ag_{1.98}(S_{1/3}Se_{1/3}Te_{1/3})$	0.80	460	168	−190	6.1	0.35	0.20	MeltAnneal, Cut, Rol	276
2023	$(Ag_{1.97}V_{0.03})(S_{0.55}Se_{0.45})$	0.71	350	200	−239	11.4	0.56	0.43	MeltAnneal, SPS	250
2023	$Ag_2(S_{0.55}Te_{0.457})$	0.39	300	431	−120	6.2	0.48	0.25	MeltAnneal, Cut	256
2023	$Ag_2(Te_{0.6}S_{0.4})$	0.80	623	205	−186	7.1	0.55	—	MeltAnneal, Cut	269
2023	$Ag_2(S_{0.5}Se_{0.5})–0.5\%Ag_2Te$	0.43	323	325	−135	5.9	0.45	0.28	MeltAnneal, MechAl, SPS	278
2022	$Ag_2(S_{0.7}Te_{0.3})$	0.80	600	185	−190	6.7	0.50	0.27	MeltAnneal, Cut	257
2022	$Ag_2(Te_{0.6}S_{0.4})$	0.80	573	357	−140	7.0	0.50	0.18	MeltAnneal, Quench, Cut	268
2022	$Ag_2((Se_{0.6}Te_{0.4})_{0.6}S_{0.4})–0.03\%Se$	0.68	470	248	−166	6.8	0.47	0.30	MeltAnneal, Cut	277
2021	$Ag_{20}(S_7Te_3)$	0.80	600	242	−169	7.0	0.51	0.28	MeltAnneal, Cut	287
2021	$Ag_2(S_{0.5}Se_{0.5})$	0.27	330	294	−118	4.1	0.50	0.30	MeltAnneal, MechAl, SPS	252
2021	$Ag_2(Se_{0.9}Te_{0.1})$	0.80	390	1100	−132	19.2	0.94	0.18	WetMechAl, SPS	263
2021	$Ag_{1.9}(S_{1/3}Se_{1/3}Te_{1/3})$	0.55	423	188	−160	4.8	0.37	0.24	MechAl, SPS	242
2020	$Ag_2SeS_{0.01}$	0.80	300	1224	−140	24.0	0.90	0.60	MeltAnneal, Cut	241
2020	$Ag_2(Se_{0.9}S_{0.1})$	0.80	358	1190	−137	22.3	1.00	0.53	MeltAnneal, SPS	260
2020	$Ag_2(Te_{0.6}S_{0.4})$	0.70	573	567	−118	7.9	0.65	—	MeltAnneal, Cut, HP	270

The units for T, σ, S, PF, and κ and κ_l are K, S cm^{-1}, μV K^{-1}, μW cm^{-1} K^{-2}, and W m^{-1} K^{-1}, respectively. Abbreviations for synthesis and processing: MeltAnneal = melting–annealing; Quench = quenching; MechAl = mechanical alloying (ball milling); ZonMelt = zone melting; WetMechAl = wet-mechanical alloying; HydS = hydrazine solution-based synthesis; SolvoS = solvothermal synthesis; Rol = rolling; SPS = spark plasma sintering; Cut = cutting; HP = hot pressing.

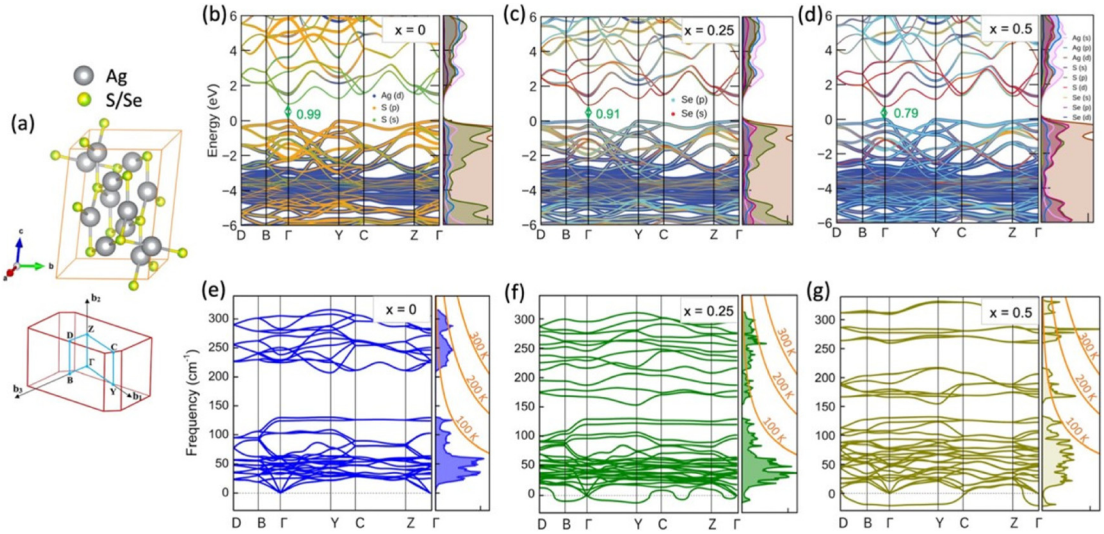

Fig. 7 (a) Crystal structure of $Ag_2(S,Se)$ solid solutions with random substitution of S and Se (yellow/green atoms) and high-symmetry points in the first Brillouin zone. (b)–(d) Projected electronic band structures and partial density-of-states of $Ag_2(S,Se)$ for different Se concentrations. (e)–(g) Phonon band structures, phonon DOS, and Bose–Einstein distribution functions (orange curves) of the non-alloyed and alloyed Se systems. Reproduced with permission from AIP Publishing ©2022.[249]

Se alloying maintains a reasonably high Seebeck coefficient (S), increases n, and thereby enhances the power factor (PF). The expected increase in electronic thermal conductivity (κ_e) is compensated by a decrease in κ_l due to the new scattering centers for phonons (Fig. 7e–g). Indeed, Hirata *et al.*[251] showed that phonons in polycrystalline Se-alloyed Ag_2S, synthesized *via* a melting and annealing method, can reach the strongest scattering limit of the Cahill model, resulting in a remarkably low κ_l of 0.4 W m^{-1} K^{-1} at RT. Notably, an additional electron density distribution appears between Ag2 sites in $Ag_2(S_{0.5}Se_{0.5})$, which suggests the presence of interstitial Ag sites. This observation implies that the number of interstitial

Ag defects increases with higher Se content. Consequently, such an increase results in a higher n, an increase in κ_e, and a reduction in κ_l.

Li *et al.*[252] demonstrated that Se alloying in polycrystalline Ag_2S optimizes the n and enhances TE performance. Furthermore, the co-alloying of Cu and Se in Ag_2S not only alters the phase composition, shifting the phase transition to 370 K, but also introduces a secondary Cu-based phase and enhances the liquid-like behavior, leading to a reduction in κ_l. As a result, Cu–Se co-alloying effectively modulates phase transition in Ag_2S, resulting in a ZT of 0.20 at 450 K. A peak ZT of 0.27 at 330 K was observed for the $Ag_2(S_{0.5}Se_{0.5})$.

Moreover, Se-alloying in Ag_2S can also benefit the extension of the cation substitution limit. For example, as shown by Wu *et al.*,[253] dual Se and Sn alloying in polycrystalline $(Ag_{1.9}Sn_{0.1})(S_{0.7}Se_{0.3})$ composition with a monoclinic Ag_2S crystal structure reduced E_g and shifted the Fermi level (E_F) into the conduction band, facilitating n-type charge transport. The computed crystal orbital Hamilton population (–COHP) for Ag–S bonding in Ag_2S and $Ag_2(S_{0.7}Se_{0.3})$ indicates that Se alloying slightly decreases this value from 1.566 eV in Ag_2S to 1.482 eV in the Se-alloyed compound. The $(Ag_{1.9}Sn_{0.1})(S_{0.7}Se_{0.3})$ composition with a high $n \approx 7.29 \times 10^{18}$ cm^{-3} and $\mu \approx 321$ cm^2 V^{-1} s^{-1} exhibited a PF of 5 μW cm^{-1} K^{-2} and a ZT of 0.42 at 343 K, while maintaining exceptional ductility exceeding 90% due to the formation of a biphasic structure that induces multiscale phonon scattering centers, resulting in a reduced κ_l of 0.18 W m^{-1} K^{-1}. Adjustment of the S/Se ratio and V-doping in polycrystalline $(Ag_{1.97}V_{0.03})(S_{0.55}Se_{0.45})$ composition with an α-Ag_2S crystal structure resulted in a ZT of 0.71 at 350 K.[250]

High-entropy materials possess a distorted lattice and diversified chemical bonding, which may significantly extend the element doping/alloying limit.[254] Indeed, the $Ag_2(S_{0.5}Te_{0.5})$ solid solution with a highly distorted crystal structure due to the large atomic size and electronegativity mismatches between S and Te extends the cation substitution limit, *i.e.*, effectively accommodates the foreign Au atoms at cation sites up to 0.07.[255] The $(Ag,Au)_2(S_{0.5}Te_{0.5})$ were composed of a mixture of cubic and amorphous phases. Substituting Ag with Au in $(Ag,Au)_2(S_{0.5}Te_{0.5})$ reduced n from 8.7×10^{18} cm^{-3} at x = 0 to 7.7×10^{17} cm^{-3} at x = 0.07. Therefore, the reduced σ and κ, combined with increased S and PF, resulted in a ZT of 0.95 at 550 K in $(Ag_{1.99}Au_{0.01})(S_{0.5}Te_{0.5})$. Notably, Au alloying had a negligible effect on the mechanical properties of $(Ag_{1.99}Au_{0.01})(S_{0.5}Te_{0.5})$, preserving a bending strain of 15%, a compressive strain of 20%, and a Vickers hardness of 20 kgf mm^{-2}.

Li *et al.*[256] synthesized an $Ag_2(S_{0.55}Te_{0.45})$ solid solution with a slight excess of Te to reduce the n. This modification enhanced the electrical transport properties and reduced the κ, resulting in a high PF of 6.2 μW cm^{-1} K^{-2} and a ZT of 0.39 at 300 K. Notably, $Ag_2(S_{0.55}Te_{0.457})$ also exhibited a high average ZT among ductile silver chalcogenides. Moreover, Te-alloying in $Ag_2(S_{0.7}Te_{0.3})$ solid solution enhanced μ, leading to a ZT of 0.80 at 600 K (Fig. 8a and b).[257] An adjustment of Ag enabled further optimization of n in $Ag_{1.9992}(S_{0.7}Te_{0.3})$, yielding a ZT of 0.85 at 550 K (Fig. 8c–f).[240] The $Ag_2(S,Te)$ solid solutions exhibited a body-centered cubic structure at 300–600 K and demonstrated superior ductility compared to Ag_2S.

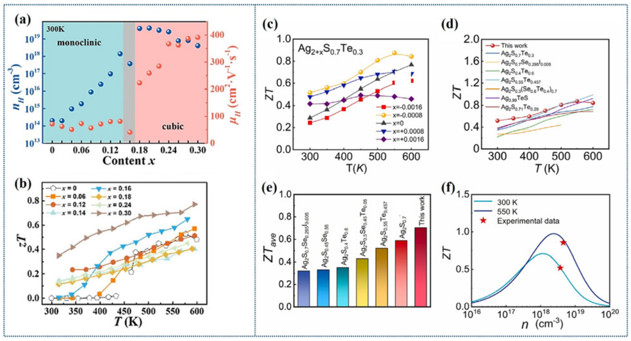

Fig. 8 (a) Te content dependence of the Hall carrier concentration (n_H) and mobility (μ_H) of $Ag_2(S,Te)$ at 300 K. ZT values of (b) $Ag_2(S,Te)$. Reproduced with permission from Elsevier ©2022.[257] (c) $Ag_{2+x}(S_{0.7}Te_{0.3})$ as a function of temperature, (d) $Ag_{1.9992}(S_{0.7}Te_{0.3})$ and reported $Ag_2(S,Te)$, and (e) $Ag_{1.9992}(S_{0.7}Te_{0.3})$ at 300–550 K, and (f) $Ag_{1.9992}(S_{0.7}Te_{0.3})$ as a function of carrier concentration at 300 K and 550 K. Reproduced with permission from Elsevier ©2024.[240]

Efforts to stabilize the cubic phase of Ag_2S at low temperatures have been undertaken by Zhong *et al.*[258] The study demonstrated that $Ag_2(S,Te)$ solid solutions can maintain a stable cubic phase at RT. These materials also exhibited excellent mechanical properties, and the $Ag_2(S_{0.8}Te_{0.2})$ composition showed a bending yield strength of 46.52 MPa at 673 K, surpassing that of Ag_2S, which declined from 80.15 MPa at 300 K to 12.66 MPa at 673 K. Notably, the $Ag_2(S_{0.7}Te_{0.3})$ solid solution achieved a high ZT of 0.59 at 723 K. Jin *et al.*[259] synthesized an $Ag_2(S_{0.7}Te_{0.3})$ solid solution *via* a zone melting technique, confirming that S and Te atoms randomly occupied the anionic sites. This composition exhibited a high $\mu \approx 410$ cm^2 V^{-1} s^{-1} and a low $\kappa_l \approx 0.2$ W m^{-1} K^{-1}, resulting in a peak ZT value of 0.30 at 600 K.

Orthorhombic Ag_2Se is brittle, whereas monoclinic Ag_2S exhibits notable ductility. Liang *et al.*[260] demonstrated that the compositional transition boundary between monoclinic and orthorhombic crystal structures in polycrystalline $Ag_2(Se_{1-x}S_x)$ occurs at x = 0.3. Substituting Se with S modifies the valence band maximum rather than the conduction band minimum, leading to an unaffected effective mass (m^*). The relatively small m^* ($0.25m_e$) in $Ag_2(S, Se)$ contributes to their high μ, thereby yielding a high ZT of 0.8 at 358 K for $Ag_2(Se_{0.9}S_{0.1})$ (Fig. 9a). Additionally, orthorhombic $Ag_2(Se_{0.9}S_{0.1})$ exhibits limited bending deformation (1.5%), whereas monoclinic $Ag_2(Se_{0.6}S_{0.4})$ demonstrates significantly higher bending deformation (~10%) without cracking. Thus, S-alloying in Ag_2Se enables the controlled formation of either an orthorhombic or monoclinic structure, offering an effective strategy for tuning its mechanical and TE properties.[233,235] A minute anion excess in polycrystalline $Ag_2SeS_{0.01}$ can also stabilize the orthorhombic structure, preventing the formation of a metastable phase in the temperature range of 300–400 K, just before the transition to the cubic phase at ~407 K.[241,261] As a result, the high n (3.5×10^{18} cm^{-3}) and μ (2030 cm^2 V^{-1} s^{-1}) contribute to

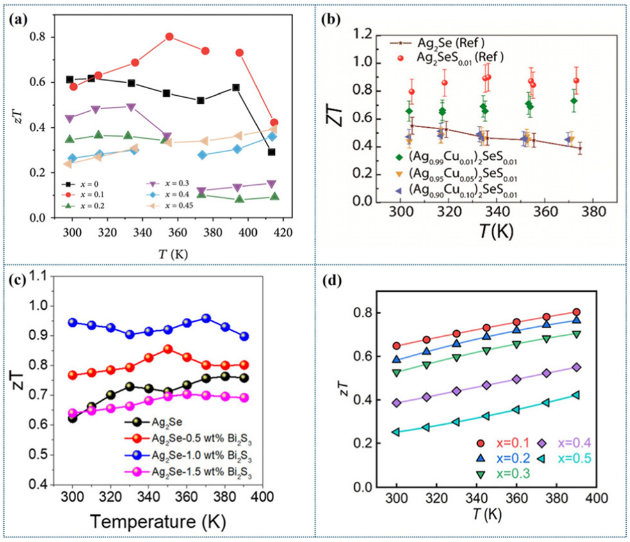

Fig. 9 Temperature-dependent *ZT* of (a) $Ag_2(Se,S)$. Reproduced with permission from the American Association for the Advancement of Science ©2020.[260] (b) $(Ag,Cu)_2(SeS_{0.01})$. Reproduced with permission from American Chemical Society ©2020.[241] (c) Ag_2Se-x wt% Bi_2S_3. Reproduced with permission from American Chemical Society ©2024.[262] (d) $Ag_2(Se,Te)$. Reproduced with permission from American Chemical Society ©2021.[263]

a high PF of 2.4 mW m^{-1} K^{-2} at 300 K. The relatively low κ leads to a *ZT* of 0.8 at 300 K in the $Ag_2SeS_{0.01}$ composition (Fig. 9b). However, during the phase transition, the orthorhombic structure becomes unstable, leading to the re-emergence of a metastable phase. Although additional cation doping with Cu further enhances the PF (~2.6 mW m^{-1} K^{-2}), the resulting increase in κ_e prevents improvement in *ZT*.

The Ag_2Se/Bi_2S_3 composites, synthesized in an aqueous solution with hydrazine as a reducing agent, exhibited an improved *S* and a slightly altered σ due to a decrease in *n* and an increase in μ, resulting from the partial substitution of Se with S.[262] The PF of the polycrystalline Ag_2Se–1.0 wt% Bi_2S_3 composite was enhanced to 2.66 mW m^{-1} K^{-2} at 370 K. Furthermore, with a decreased κ due to the effective phonon scattering both at point defects and interphase boundaries, *ZT* values of the Ag_2Se–1.0 wt% Bi_2S_3 composites were improved up to 0.96 at 370 K (Fig. 9c).

DFT calculations and single parabolic band (SPB) modeling of Te-doped Ag_2Se indicate that the reduced contribution of Se 4p orbitals to the total density of states decreases the carrier effective mass (m^*) with increasing Te content. This reduction, along with dense phonon dispersion, is expected to enhance the theoretical *ZT*.[263] The decrease in m^* reduces the *S* but increases the σ. However, the deformation potential (E_{def}) also rises with increasing Te content, suppressing μ. Despite this, the reduced m^* still contributes to an enhancement of PF. Thus, the theoretical peak *ZT* exceeds 1.0 in the $Ag_2(Se_{0.9}Te_{0.1})$ composition at $n = 7.0 \times 10^{17}$ cm^{-3}.

Moreover, SPB modeling predicts that theoretical *ZT* values above 1.1 at 300 K are achievable for $Ag_2(Se_{0.7}Te_{0.3})$ composition at $n = 4.0 \times 10^{17}$ cm^{-3}. Ternary $Ag_2(Se,Te)$ solid solutions, synthesized *via* wet-mechanical alloying and SPS, also exhibited high Te solubility (~50%).[263] The as-sintered ternary $Ag_2(Se,Te)$ solid solutions demonstrated complex microstructures, including dislocations, nanograins, grain boundaries, Te_{Se} substitution, lattice distortions, and localized strain, which contribute to strong phonon scattering and result in ultralow κ_l values of 0.21–0.31 W m^{-1} K^{-1} at 300 K. The *ZT* of 0.65–0.80 was observed in the $Ag_2(Se_{0.9}Te_{0.1})$ solid solution at 300–390 K (Fig. 9d).

The modulation of the anion ratio in Ag-based materials enhances their thermoelectric and mechanical properties. However, it also introduces phase complexity and multiple structural transitions, necessitating precise control to maintain stable TE parameters upon heating. Recently, Li *et al.*[264] demonstrated that the $Ag_2(Te,S)$ solid solutions consist of both amorphous and crystalline phases at 20–420 K. The Ag_2Te-based phase retains its amorphous state within the 20–300 K range, whereas the amorphous Ag_2S-based phase begins to crystallize below 183 K. Notably, in $Ag_2(S_{0.4}Te_{0.6})$, the presence of an amorphous Ag_2S-based phase at 183–420 K ensures excellent ductility and low κ_l, yielding a *ZT* of 0.17 at 300 K. During the heat treatment of $Ag_2(Te,S)$ solid solutions,[265] three crystal phases can emerge: a low-temperature crystalline phase, an amorphous phase, and a high-temperature cubic phase. The high-temperature cubic phase transforms into the low-temperature crystalline phase with the formation of a metastable amorphous phase, enhancing σ below the phase transition temperature. The $Ag_2(Te_{0.5}S_{0.5})$ compound, annealed at 473 K, exhibited a *ZT* of 1.02 at 623 K, which increased to 1.34 at 523 K during the second heating cycle.

A variety of strengthening methods, including alloying, grain refinement, and secondary phase precipitation, have been employed to tune the mechanical properties of TE materials.[266] In this context, understanding the relationship between phase composition and mechanical properties in Ag-based TE materials is crucial for elucidating the mechanisms underlying their exceptional ductility. The analysis of mechanical properties in Te-rich $Ag_2(Te,S)$ solid solutions by Wang *et al.*[267] revealed a brittle–ductile transition. High ductility was observed in Ag_2Te crystals with the monoclinic and cubic phases, previously considered brittle. The ductile $Ag_2(Te_{0.9}S_{0.1})$ exhibited a *ZT* of 0.6 at 600 K. The removal of the monoclinic Ag_2Te phase in the $Ag_2(Te,S)$ compositions increased compressive strain, exceeding 70%.

A high tensile elongation of 107% was achieved in $Ag_2(Te_{0.7}S_{0.3})$ solid solutions.[268] Moreover, the high mobility ($\mu \approx 1000$ cm^2 V^{-1} s^{-1} at 300 K) results in a *ZT* value of 0.8 at 573 K for the annealed $Ag_2(Te_{0.6}S_{0.4})$. The reversible brittle–ductile transition in $Ag_2(Te_{0.6}S_{0.4})$ was demonstrated by tuning the phase composition through heat treatments.[269] The $Ag_2(Te_{0.6}S_{0.4})$, annealed at 973 K for 7 days, exhibits an amorphous/cubic structure and shows a compressive strain exceeding 80%, with an engineering stress of 600 MPa. In addition to its superior plasticity, $Ag_2(Te_{0.6}S_{0.4})$ demonstrates excellent TE properties, attaining a high *ZT* of 0.8 at 673 K.

The flexibility and high TE performance of $Ag_2(Te_{0.6}S_{0.4})$ were achieved by He *et al.*[270] through amorphization. Amorphization in the S-doped $Ag_2(Te_{0.6}S_{0.4})$ composition contributed to excellent mechanical properties, including a bending strain above 14% under a stress of 110 MPa, an elastic strain limit of 2% under 70 MPa, a compression strain of 25%, a tensile strain of 12.5%, and a Vickers hardness of 19.5 kgf mm^{-2}. The coexistence of amorphous and crystalline phases contributed to exceptional flexibility and a low κ of 0.65 W m^{-1} K^{-1} at 573 K. A high μ (750 cm^2 V^{-1} s^{-1}) and n (8.6×10^{18} cm^{-3}) led to a high PF of 7.9 μW cm^{-1} K^{-2} and a peak ZT of 0.7 at 573 K surpassing that of organic TE materials.[271]

The Ag_2Te/Ag_2S composites, synthesized *via* a low-cost solvothermal method and SPS, exhibited a tunable phase composition, optimizing both n and μ. In particular, $Ag_2(S_{0.8}Te_{0.2})$, with a phase distribution of Ag_2Te (95.06%) and Ag_2S (4.94%), demonstrated ZT values of 0.42 at 373 K and 0.38 at 298 K.[272] The enhanced ZT in these composites results from reduced κ_l, facilitated by phonon scattering at the branched vein-like microstructure, amorphous transition phase boundaries, and dislocations. The addition of Ag_2S improved the plasticity of the Ag_2S/Ag_2Te composites, achieving a band strain of 2.5%. Also, n increased from 10^{14} cm^{-3} (in Ag_2S) to 10^{18} cm^{-3} (in $Ag_2(S_{0.8}Te_{0.2})$), while μ reached 5436 cm^2 V^{-1} s^{-1}, 1.86 times higher than that of Ag_2Te.

Doping at the anion site has been widely investigated for the synthesis of high-entropy chalcogenide compounds featuring metastable phases.[273,274] The first-principles calculations by Biswas *et al.*[275] predict an enhanced power factor in the pseudo-ternary $Ag_2(Se_{0.5}Te_{0.25}S_{0.25})$ phase, driven by spin-dependent band splitting known as the Rashba effect following S and Te substitution. Consequently, increased configurational entropy theoretically predicts a low κ_l (0.34 W m^{-1} K^{-1}) and a high ZT of 2.1 at 400 K.

The efforts to stabilize the high-temperature cubic β-Ag_2S phase through entropy engineering[239] have successfully resulted in the formation of single-phase $Ag_2(S,Se,Te)$ compounds at RT, exhibiting superior mechanical properties, including ductility. Notably, the mixed-anion $Ag_{1.98}(S_{0.34}Se_{0.33}Te_{0.33})$ with slight Ag deficiency demonstrated an optimized σ, reduced κ, and a significantly enhanced ZT value of 0.85 at 500 K. These improvements in TE parameters are attributed to optimized configurational entropy, strong anharmonicity, and weakened ionic bonding, which collectively yield a high $n \approx 10^{18}$–10^{19} cm^{-3} and $\mu \approx 826$ cm^2 V^{-1} s^{-1} at $x = 0.33$.

Chen *et al.*[276] identified the compositional region of the cubic phase (Fig. 10) and proposed an anion-site alloyed $Ag_{1.98}(S_{1/3}Se_{1/3}Te_{1/3})$ with the highest configurational entropy (ΔS). This anion-site alloying not only enhanced the mechanical properties of $Ag_{1.98}(S_{1/3}Se_{1/3}Te_{1/3})$ but also improved its TE performance, achieving an ultralow κ_l of 0.2 W m^{-1} K^{-1} and a high ZT of 0.8 at 460 K. Notably, the material exhibits a tensile strain of 97%.

Yu *et al.*[242] synthesized an $Ag_{1.9}(Se_{1/3}S_{1/3}Te_{1/3})$ solid solution using high-energy ball milling followed by SPS. The anion-site alloying of Se, S, and Te significantly enhances phonon scattering, resulting in an ultralow κ_l of 0.2 W m^{-1} K^{-1}. Additionally, sulfur volatilization during the SPS process induces porosity in the material, which further contributes to phonon scattering. Consequently, a peak ZT of 0.55 was observed at 423 K.

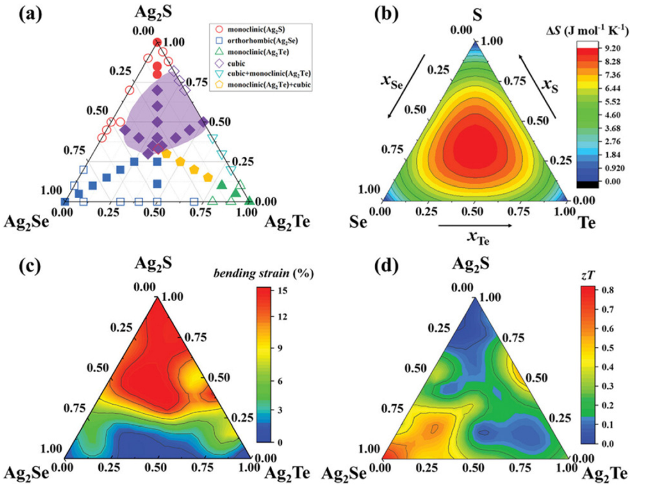

Fig. 10 (a) Schematic phase diagram of Ag_2X (X = S, Se, Te). (b) Calculated configurational entropy ΔS considering the mixture of S/Se/Te at the anion site. (c) Phase diagram of maximum bending strain at room temperature of the Ag_2S–Ag_2Se–Ag_2Te system. (d) Phase diagram of the room-temperature ZT value of the Ag_2S–Ag_2Se–Ag_2Te system. Reproduced with permission from Wiley-VCH GmbH ©2024.[276]

To extend the operating temperature range of Ag(S,Se,Te), Xie *et al.*[277] alloyed $Ag_2(Se_{0.6}Te_{0.4})$ with Ag_2S to stabilize the cubic phase within the temperature range of 300–470 K. This alloying effect lowers the orthorhombic-to-cubic phase transition temperature, enabling $Ag_2(S_{0.4}(Se_{0.6}Te_{0.4})_{0.6})$ to maintain a stable body-centered cubic (bcc) structure. Also, $Ag_2(S_{0.4}(Se_{0.6}Te_{0.4})_{0.6})$ demonstrates remarkable mechanical properties, sustaining a bending strain exceeding 11% before fracture, in contrast to $Ag_2(Se_{0.6}Te_{0.4})$, which exhibits a strain below 1%. Despite its stable cubic structure and excellent ductility, the $Ag_2(S_{0.4}(Se_{0.6}Te_{0.4})_{0.6})$ solid solution has an extremely high carrier concentration ($n \approx 3.1 \times 10^{19}$ cm^{-3} at RT), leading to a low ZT of 0.06. To improve its TE performance, a small amount of excess Se was introduced into the $Ag_2(S_{0.4}(Se_{0.6}Te_{0.4})_{0.6})$, effectively reducing the carrier concentration by an order of magnitude. This modification decreased both σ and κ_e, while significantly enhancing S, resulting in a peak ZT of 0.68 at 470 K.

Wu *et al.*[278] synthesized a polycrystalline $Ag_2(S_{0.5}Se_{0.5})$ matrix with 0.5 mol% Ag_2Te inclusions, achieving a ZT of 0.43 at 323 K and a high bending strain of 32.5%. The incorporation of Ag_2Te optimized the n and μ, resulting in a high PF of 6 μW cm^{-1} K^{-2}. Furthermore, Ag_2Te induced the formation of Ag-poor amorphous phase boundaries, significantly enhancing the overall plasticity. These amorphous phase boundaries, combined with multiscale phonon scattering mechanisms, effectively lowered the κ_l to 0.28 W m^{-1} K^{-1} at 323 K. DFT calculations revealed that the intrinsic n-type conductivity of Ag_2S

and $Ag_2(S_{0.5}Se_{0.5})$ is attributed to S and Se vacancies, as well as Ag interstitials. Additionally, Ag_2Te results in amorphous phase boundaries that, along with multiscale phonon scattering centers, contribute to the reduction in κ_l.

The conventional method to synthesize Ag-based chalcogenides predominantly involves solid-state reactions, including melting, annealing, and subsequent quenching. The obtained ingots are typically cut into pieces or ground into powder, followed by SPS to achieve densified TE elements. However, this approach has limitations for large-scale production, whereas techniques such as hot-rolling could facilitate the fabrication of TE elements with a larger surface area. Recently, orthorhombic $Ag_2(Se,S)$ films with outstanding mechanical properties (Fig. 11) were successfully fabricated by hot-rolling bulk materials at 393 K.[279] This approach promotes the formation of dense dislocations and grain refinement and increases the elastic strain while ensuring the recovery of TE properties even after 10^5 bending cycles. A maximal power output of 157 μW, corresponding to a specific power density of 5 μW cm^{-1} K^{-2}, was achieved in the $Ag_2(Se_{0.9}S_{0.1})$ solid solution at a temperature difference of 76 K. Another example is

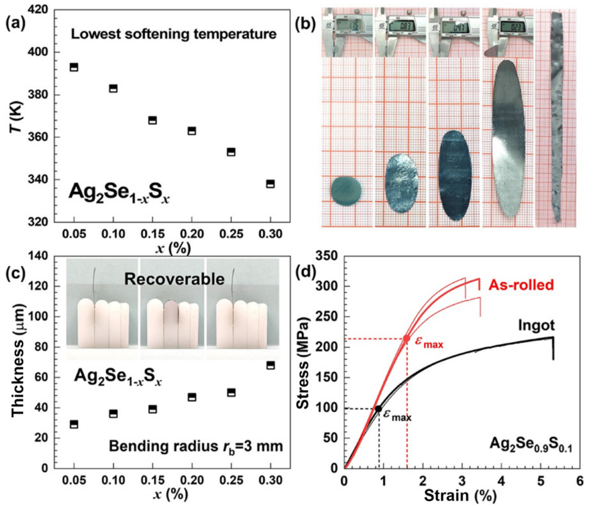

Fig. 11 (a) Softening temperature of $Ag_2(Se,S)$ alloys. (b) Dimensional evolution for $Ag_2(Se_{0.9}S_{0.1})$ by multipass hot rolling. (c) Elasticity of $Ag_2(Se,S)$ alloys. (d) Stress *versus* strain for $Ag_2(Se_{0.9}S_{0.1})$ bulks with and without hot-rolling. Reproduced with permission from American Chemical Society ©2024.[279]

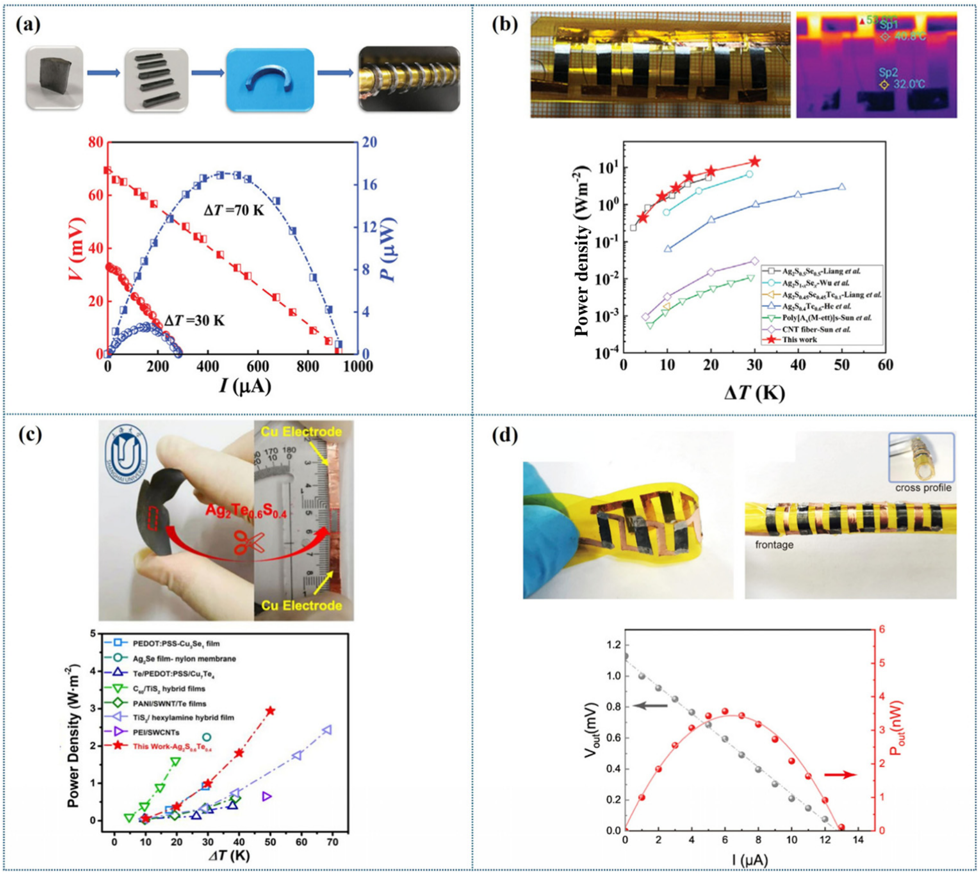

Fig. 12 (a) Hetero-shaped $Ag_{20}(S_7Te_3)$-based TEG and its output *V*–*I*, *P*–*I* characteristics. Reproduced with permission from Wiley-VCH GmbH ©2021.[287] (b) Flexible in-plane $Ag_{1.98}(S_{1/3}Se_{1/3}Te_{1/3})$-Pt-based TEG and power density *vs*. Δ*T* compared to typical flexible TEGs. Reproduced with permission from Wiley-VCH GmbH ©2024.[276] (c) $Ag_2(Te_{0.6}S_{0.4})$-based TEG and power density *vs*. Δ*T* compared to typical flexible TEGs. Reproduced with permission from the American Association for the Advancement of Science ©2020.[270] (d) Flexible $Ag_2(S_{0.6}Se_{0.3}Te_{0.1})$ foil-based TEG and its output *V*–*I*, *P*–*I* characteristics at a heat source temperature of 37 °C. Reproduced with permission from American Chemical Society ©2022.[288]

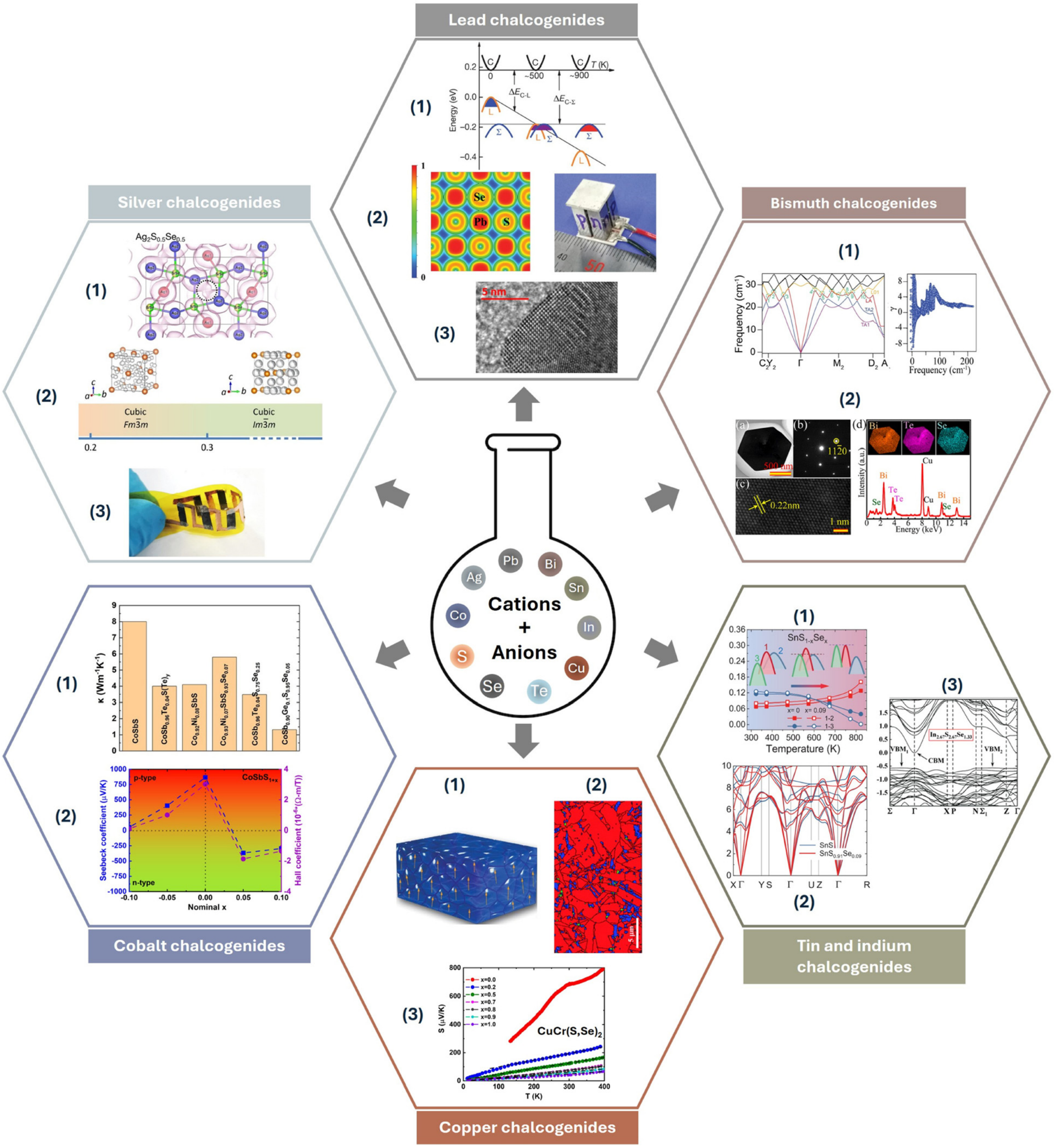

Fig. 13 Outlook of the effects of anion mixing on thermoelectric metal chalcogenides. **Lead chalcogenides**: (1) electronic band convergence. Adapted with permission from Springer Nature ©2011;[46] (2) higher covalency and hardness, π-type TEGs. Adapted with permission from The Royal Society of Chemistry ©2020 (License CC BY 3.0);[47] (3) multiscale defects (*e.g.*, nano precipitates, strains). Adapted with permission from Elsevier ©2017.[52] **Bismuth chalcogenides**: (1) alloying for higher anharmonicity. Adapted with permission from Wiley-VCH GmbH ©2022;[58] (2) nanostructuring and interface engineering. Adapted with permission from American Chemical Society ©2016.[62] **Tin and indium chalcogenides**: (1) tuning phase transitions and band structures; (2) softening phonon band structures. Adapted with permission from the American Association for the Advancement of Science ©2019;[85] (3) band structure engineering. Adapted with permission from The Royal Society of Chemistry ©2021 (License CC BY 3.0).[94] **Copper chalcogenides**: (1) nanoscale mosaicity. Adapted with permission from Wiley-VCH GmbH ©2015;[111] (2) selectivity and control of phase composition. Adapted with permission from The Royal Society of Chemistry ©2017 (License CC BY 3.0);[127] (3) semiconductor-to-metal transition. Adapted with permission from Wiley-VCH GmbH ©2023.[152] **Cobalt chalcogenides**: (1) softening of the acoustic phonons. Adapted with permission from The Royal Society of Chemistry ©2024 (License CC BY 3.0);[220] (2) tuning the p-type to n-type conductivity transition. Adapted with permission from AIP Publishing ©2022 (License CC BY).[224] **Silver chalcogenides**: (1) tuning Ag interstitial defects. Adapted with permission from AIP Publishing ©2023 (License CC BY);[251] (2) adjusting the crystal structure, phase transitions, and ductility. Adapted with permission from Elsevier ©2024;[267] (3) prototyping TEGs. Adapted with permission from American Chemical Society ©2022.[288]

the fabrication of $Ag_2(Te,S)$ films *via* hot-rolling at 393 K, exhibiting an increased elastic strain of 1.8% in $Ag_2(Te_{0.8}S_{0.2})$, representing a 200% enhancement compared to unalloyed Ag_2Te.[280]

The solid solutions between Ag_2Te and Ag_2Se also demonstrated remarkable mechanical and TE properties,[281] a maximum compressive strain rate of 36%, a compressive yield strength of 180 MPa, and a Vickers hardness of 0.63 GPa in the $Ag_2(Te_{0.8}Se_{0.2})$ bulks with a *ZT* of 0.3 at 300 K and 0.4 at 380 K. Wang *et al.*[282] reported a unique room-temperature plastic deformation mechanism in inorganic semiconductors $Ag_2(Te,S)$, driven by sublattice amorphization coupled with Ag-ion diffusion.

The demonstrated high-performance Ag-based materials for flexible and wearable TEGs are promising to replace the costly and toxic Bi_2Te_3-based materials for thermal energy harvesting applications. A prototype of the TEG was successfully fabricated using ductile n-type $Ag_2(S_{0.55}Se_{0.55})$ and over-stoichiometric p-type $Cu_{2.075}Se$ materials with a *ZT* value of 0.5 at 300 K. The monolithic TEG with negligible Ag- or Cu-ion migration exhibited a maximum power density of 0.68 mW cm^{-2} at ΔT = 30 K.[283] The ultra-flexible TEG with 6 legs assembled with a Se-substituted Ag_2S film on a nylon membrane demonstrated a power density of 0.66 mW cm^{-2} at a temperature difference of 28.8 K.[284]

Owing to its superb flexibility and high TE performance, $Ag_2(Te_{0.6}S_{0.4})$ was utilized to develop a prototype of 3D wearable fabric, achieving a normalized power density of 0.4 μW m^{-1} K^{-2} at ΔT = 20 K.[285] The effectiveness of orthorhombic Ag_2Se and monoclinic Ag_2S nanocomposites, synthesized *via* a solvothermal method on carbon fabric, was demonstrated in a 2-pair TE module, which showed an output voltage from 0.1 to 7.4 mV at ΔT = 3–8 K.[286]

The prototype TEG, consisting of 10 $Ag_{20}(S_7Te_3)$ strips, exhibited an open-circuit voltage of 69.2 mV and a maximum power output of 17.1 μW at a temperature difference of 70 K (Fig. 12a).[287] The entropy-engineered $Ag_2(S_{1/3}Se_{1/3}Te_{1/3})$ can be readily rolled into flexible thin films. A six-leg in-plane device was fabricated using this material, achieving an output voltage of 13.6 mV, a maximum power of 12.8 μW, and a power density of 14.3 W m^{-2} at a temperature difference of 30 K (Fig. 12b).[276] A flexible in-plane device with a single leg based on the amorphized $Ag_2(Te_{0.6}S_{0.4})$ produced a power of 3.5 μW at a temperature difference of 50 K, demonstrating its great potential as a self-powered TE generator (Fig. 12c).[270] The large-scale all-inorganic silver chalcogenide foils were produced using a rolling process by Liang *et al.*[288] A high *ZT* of 0.47 at 310 K was achieved for $Ag_2(S_{0.45}Se_{0.45}Te_{0.1})$ composition. A proof-of-concept flexible TE generator based on these silver chalcogenide foils demonstrated an open-circuit voltage of 1.19 mV and an output power density of 1.8 mW m^{-2} with a temperature difference of 2.7 K (Fig. 12d).

Beyond binary Ag-based compounds, multicomponent silver-bearing minerals deserve particular attention, including the argyrodites Ag_8SnSe_6,[289] Ag_8GeSe_6,[290] and Ag_8SiSe_6,[291] as well as the pavonites $AgBi_3S_5$,[292] $Ag_3Pb_4Bi_{11}Se_{22}$,[293] and $Ag_{1.75}InSb_{5.75}Se_{11}$.[294] In particular, Ag-based superionic argyrodites have attracted considerable attention owing to their liquid-like ultralow κ_l supporting the PLEC concept. For instance, n-type cubic argyrodites $Ag_4M_{0.5}S_2Te$ (M = Sn, Ge) exhibit an ultralow κ of 0.30 W m^{-1} K^{-1}, attributed to large lattice anharmonicity arising from triangular, rod-like, and cage-like cluster units alongside weakly bonded Ag^+ ions. Optimization *via* generating Te deficiency enhances the PF to 2.61 μW cm^{-1} K^{-2}, yielding a peak *ZT* of 0.74 at 823 K.[295] Substituting Te for S increases the atomic mass and weakens the chemical bonds, leading to a substantial reduction in sound velocities. Through this lattice-softening approach, the thermal conductivity of $Ag_8Sn(S,Te)_6$ reaches 0.15–0.26 W m^{-1} K^{-1} at RT.[296] Substituting Se for S in polycrystalline $Ag_8Sn(S,Se)_6$ shifts the orthorhombic-cubic phase transition, expanding the temperature range of the thermoelectrically favored cubic phase. A peak *ZT* of 0.80 at 773 K is achieved for $Ag_8Sn(S_{0.97}Se_{0.03})_6$.[297] Wu *et al.* synthesized $AgBi_3(Se,S)_5$ solid solutions. Se/S anion mixing in $AgBi_3(Se,S)_{5.08}$ simultaneously increases configurational entropy, enhancing phonon point defect scattering and reducing κ_l to 0.45 W m^{-1} K^{-1}, and modifies the effective mass near the Fermi level, boosting electrical transport. As a result, polycrystalline $AgBi_3(Se_{0.9}S_{0.1})_{5.08}$ achieves a peak *ZT* of 0.42 at 723 K.[298]

7. Conclusions and outlook

This perspectival review has highlighted the advances in enhancing the thermoelectric performance of metal chalcogenides utilizing the anion-mixed scheme at the chalcogenide (S, Se, Te) site. The material families covered span from the traditional Pb-, Bi-, Sn- and In-based systems to the currently strongly emerging Cu-, Co-, and Ag-based materials (Fig. 13). Compared to the so-called mixed-anion frameworks, the anion mixing approach realized through solid-solution formation, which was the focus of this review, is in general better suited for the systematic optimization of electrical transport, because it enables continuous tuning of the band structure without fundamentally altering the host crystal structure. On the other hand, in the mixed-anion frameworks, stronger intrinsic phonon scattering and lower lattice thermal conductivities are often seen. However, it should be emphasized that ultralow lattice thermal conductivity values have also been achieved through the substitutional solid solution anion-mixing approach.

Anion mixing can also increase both anion and cation solubility limits, as was, for example, observed in entropy-driven Pb(S,Se,Te) solid solutions. This expands the accessible carrier concentration range, enables effective band gap tuning, and enhances phonon scattering through strong atomic mass contrast. The extent of S/Se/Te miscibility naturally varies across material families due to differences in the host crystal structure, site symmetry, and the tolerance of the cation sublattice to anion size mismatch, all of which govern the thermodynamic stability of the resulting solid solution.

Besides the anion mixing approach, another common chemical tuning approach applied to enhance the thermoelectric properties of metal chalcogenides is cation doping; these efforts have been briefly summarized as well in the present review for each metal chalcogenide material family. A distinct difference between the anion-mixing and cation doping/substitutions is that anion mixing at the S/Se/Te site is of the isovalent substitution type, while the most effective cation substitutions are often aliovalent. Nevertheless, isovalent anion substitution may also modify the cation-site defect equilibria, as was, for example, demonstrated in the case of In-based chalcogenides, where isovalent S-for-Se substitution was found to suppress the annihilation of donor defects and thereby enhance the electrical conductivity. In copper chalcogenides, anion mixing was found to stabilize Cu^+ within its sublattice, thereby improving operational stability and fine-tuning the charge carrier transport; moreover, the resulting point defects provided additional phonon scattering centers, further reducing thermal conductivity and enhancing the thermoelectric performance.

In the present review, the anion-mixing effects were discussed in detail in separate sections both for the state-of-the-art Pb-, Bi-, Sn- and In-based systems and a number of currently strongly emerging Cu-, Co-, and Ag-based thermoelectrics. For lead chalcogenides, anion mixing was found to improve charge transport by promoting band convergence, enabling a better band gap, carrier concentration and effective mass control, and suppressing bipolar effects. Simultaneously, the resulting crystal disorder, point defects, lattice strain, and nanostructures enhance phonon scattering and reduce lattice thermal conductivity. Moreover, through tailored cation–anion bridges, decoupling of electron and phonon transport becomes possible. In bismuth chalcogenides, anion mixing enables control over the conductivity type, carrier concentration, and band gap, thereby suppressing bipolar effects. In tin and indium chalcogenides, anion mixing tunes carrier concentration and the valence band structure, increasing the density of states and improving electrical transport. At the same time, the induced defects and hierarchical microstructure strengthen phonon scattering, lower lattice thermal conductivity, and may stabilize thermoelectrically favorable phases.

The recent renewed interest in copper chalcogenides is largely due to their low lattice thermal conductivity which mainly arises from the liquid-like Cu^+ sublattice; the trade-off is that this ion migration also causes phase instability. Here, impressively, the anion-mixing approach provided an effective way to not only stabilize the Cu sublattice by suppressing the Cu-vacancy formation but also to lower thermal conductivity and enhance the thermoelectric performance through strain-induced phonon scattering and an optimized electronic structure and carrier concentration. Cobalt chalcogenides, particularly the CoSbX compounds, offer a stable framework where anion mixing has been shown to induce phonon softening and strong scattering and accordingly reduce thermal conductivity. Interestingly, the electrical conductivity type of the CoSbX materials can be tuned by composition, enabling p–n module design, though challenges such as bipolar conduction still remain. In silver chalcogenides, anion mixing is an effective strategy for tuning both the thermoelectric and mechanical properties. In Ag_2X compounds, low lattice thermal conductivity mainly arises from structural disorder and liquid-like Ag-ion motion, while anion substitutions further enhance phonon scattering through defects, strain, phase boundaries, and multiscale microstructures. Simultaneously, anion mixing tunes the band gap, carrier effective mass, and defect chemistry, thereby optimizing the carrier concentration, mobility, and power factor. Because cation substitution is often limited in these systems, anion mixing is valuable for expanding the compositional flexibility, stabilizing favorable phases, shifting structural transitions, and controlling crystallinity or partial amorphization. These effects make mixed-anion Ag-based chalcogenides promising for flexible devices, although further work is needed to improve the stability of practical prototypes.

Overall, metal chalcogenides provide an excellent platform in which anion mixing may function as a targeted strategy to simultaneously manipulate electron and phonon transport. Varying the S/Se/Te composition allows electronic structure tuning (control over the band gap, band alignment, band convergence, and carrier effective mass) needed to increase the power factor. In parallel, the created anion disorder may introduce mass fluctuation, local strain, and hierarchical microstructural heterogeneity, which is highly beneficial to enhance phonon scattering and suppress lattice thermal conductivity. Beyond the electronic and thermal transport tuning, anion mixing also regulates defect chemistry by modifying point defect formation energies, charge compensation, solubility limits, and secondary phase formation, while in many systems, it additionally drives phase stabilization or polymorphic transitions that can unlock the thermoelectrically favorable states. However, these benefits are not necessarily universal: excessive disorder may reduce carrier mobility, incomplete alloying may lead to phase separation, and structurally stabilized phases do not always yield superior thermoelectric performance. A deeper mechanistic understanding of how anion mixing couples electronic structure, defect chemistry, and phase stability should further accelerate the development of high-performance and especially tellurium-lean metal chalcogenide thermoelectrics so that mixed-anion metal chalcogenides could become key thermoelectric materials for sustainable energy technologies.

Author contributions

The manuscript was written through contributions of all authors.

Conflicts of interest

There are no conflicts of interest to declare.

Data availability

No primary research results, software or code have been included and no new data were generated or analysed as part of this review.

Acknowledgements

Funding was received from the Research Council of Finland (367417).

References

1 G. J. Snyder and E. S. Toberer, *Nat. Mater.*, 2008, **7**, 105–114.

2 B. Poudel, Q. Hao, Y. Ma, Y. Lan, A. Minnich, B. Yu, X. Yan, D. Wang, A. Muto, D. Vashaee, X. Chen, J. Liu, M. S. Dresselhaus, G. Chen and Z. Ren, *Science*, 2008, **320**, 634–638.

3 J. Wei, L. Yang, Z. Ma, P. Song, M. Zhang, J. Ma, F. Yang and X. Wang, *J. Mater. Sci.*, 2020, **55**, 12642–12704.

4 H. Ming, Z.-Z. Luo, Z. Zou and M. G. Kanatzidis, *Chem. Rev.*, 2025, **125**, 3932–3975.

5 H. Kleinke, *Chem. Mater.*, 2010, **22**, 604–611.

6 M. Elgendi, A. E. Kabeel and F. A. Essa, *Alexandria Eng. J.*, 2023, **65**, 963–982.

7 L. Huang, Y. Zheng, L. Xing and B. Hou, *Therm. Sci. Eng. Prog.*, 2023, **45**, 102064.

8 N. Jaziri, N. Gutzeit, H. Bartsch, A. Boughamoura, J. Müller and F. Tounsi, *Sustainable Energy Fuels*, 2022, **6**, 2330–2342.

9 K.-W. Du and C.-I. Wu, *Appl. Sci.*, 2024, **14**, 685.

10 Y. Wang, Y. Shi, D. Mei and Z. Chen, *Appl. Energy*, 2018, **215**, 690–698.

11 N. Swarnkar, *JETIR*, 2019, **6**, 131.

12 *CRC Handbook of Thermoelectrics*, ed. D. M. Rowe, CRC Press, Boca Raton, FL, 1995.

13 J. He and T. M. Tritt, *Science*, 2017, **357**, 1369.

14 J. Yang, H.-L. Yip and A. K.-Y. Jen, *Adv. Energy Mater.*, 2013, **3**, 549–565.

15 A. D. LaLonde, Y. Pei, H. Wang and G. J. Snyder, *Mater. Today*, 2011, **14**, 526–532.

16 J. Xin, Y. Tang, Y. Liu, X. Zhao, H. Pan and T. Zhu, *npj Quantum Mater.*, 2018, **3**, 9.

17 G. Li, J. García, D. L. Ramos, V. Barati, N. Pérez, I. Soldatov, H. Reith, G. Schierning and K. Nielsch, *Nat. Electron.*, 2018, **1**, 555–561.

18 J. Qiu, Y. Yan, T. Luo, K. Tang, L. Yao, J. Zhang, M. Zhang, X. Su, G. Tan, H. Xie, M. G. Kanatzidis, C. Uher and X. Tang, *Energy Environ. Sci.*, 2019, **12**, 3106–3117.

19 G. Tan, L.-D. Zhao and M. G. Kanatzidis, *Chem. Rev.*, 2016, **116**, 12123–12149.

20 M. N. Hasan, H. Wahid, N. Nayan and M. S. M. Ali, *Int. J. Energy Res.*, 2020, **44**, 6170–6222.

21 I. U. I. Ravich, B. A. Efimova and I. A. Smirnov, *Semiconducting lead chalcogenides*, Plenum Press, New York, 1970.

22 R. F. Brebrick and R. S. Allgaier, *J. Chem. Phys.*, 1960, **32**, 1826–1831.

23 J. Zhang, D. Wu, D. He, D. Feng, M. Yin, X. Qin and J. He, *Adv. Mater.*, 2017, **29**, 1703148.

24 J. He, S. N. Girard, J. C. Zheng, L. Zhao, M. G. Kanatzidis and V. P. Dravid, *Adv. Mater.*, 2012, **24**, 4440–4444.

25 L. Yang, Z.-G. Chen, M. Hong, L. Wang, D. Kong, L. Huang, G. Han, Y. Zou, M. Dargusch and J. Zou, *Nano Energy*, 2017, **31**, 105–112.

26 S. N. Girard, J. He, X. Zhou, D. Shoemaker, C. M. Jaworski, C. Uher, V. P. Dravid, J. P. Heremans and M. G. Kanatzidis, *J. Am. Chem. Soc.*, 2011, **133**, 16588–16597.

27 B. Xu, M. Agne, T. Feng, T. Chasapis, X. Ruan, Y. Zhou, H. Zheng, J.-H. Bahk, M. Kanatzidis, J. Snyder and Y. Wu, *Adv. Mater.*, 2017, **29**, 1605140.

28 T. Fu, X. Yue, H. Wu, C. Fu, T. Zhu, X. Liu, L. Hu, P. Ying, J. He and X. Zhao, *J. Materiomics*, 2016, **2**, 141–149.

29 Y. Wu, Z. Chen, P. Nan, F. Xiong, S. Lin, X. Zhang, Y. Chen, L. Chen, B. Ge and Y. Pei, *Joule*, 2019, **3**, 1276–1288.

30 P. K. Rawat, B. Paul and P. Banerji, *ACS Appl. Mater. Interfaces*, 2014, **6**, 3995–4004.

31 M. R. Shankar and A. N. Prabhu, *J. Mater. Sci.*, 2023, **58**, 16591–16633.

32 H. Wang, Y. Pei, A. D. LaLonde and G. J. Snyder, *Adv. Mater.*, 2011, **23**, 1366–1370.

33 M. Hong, Z.-G. Chen, S. Matsumura and J. Zou, *Nano Energy*, 2018, **50**, 785–793.

34 C. Zhou, Y. Yu, Y.-L. Lee, B. Ge, W. Lu, O. Cojocaru-Mirédin, J. Im, S.-P. Cho, M. Wuttig and Z. Shi, *J. Am. Chem. Soc.*, 2020, **142**, 15172–15186.

35 C. Zhou, Y. Yu, Y. K. Lee, O. Cojocaru-Mirédin, B. Yoo, S.-P. Cho, J. Im, M. Wuttig, T. Hyeon and I. Chung, *J. Am. Chem. Soc.*, 2018, **140**, 15535–15545.

36 L. Hu, Y.-W. Fang, F. Qin, X. Cao, X. Zhao, Y. Luo, D. V. M. Repaka, W. Luo, A. Suwardi, T. Soldi, U. Aydemir, Y. Huang, Z. Liu, K. Hippalgaonkar, G. J. Snyder, J. Xu and Q. Yan, *Nat. Commun.*, 2021, **12**, 4793.

37 L.-D. Zhao, J. He, S. Hao, C.-I. Wu, T. P. Hogan, C. Wolverton, V. P. Dravid and M. G. Kanatzidis, *J. Am. Chem. Soc.*, 2012, **134**, 16327–16336.

38 L.-D. Zhao, J. He, C.-I. Wu, T. P. Hogan, X. Zhou, C. Uher, V. P. Dravid and M. G. Kanatzidis, *J. Am. Chem. Soc.*, 2012, **134**, 7902–7912.

39 Y. Qin, Y. Xiao, D. Wang, B. Qin, Z. Huang and L.-D. Zhao, *J. Alloys Compd.*, 2020, **820**, 153453.

40 Z.-Z. Luo, S. Cai, S. Hao, T. P. Bailey, H. Xie, T. J. Slade, Y. Liu, Y. Luo, Z. Chen and J. Xu, *J. Am. Chem. Soc.*, 2022, **144**, 7402–7413.

41 M. Zhao, C. Chang, Y. Xiao, R. Gu, J. He and L.-D. Zhao, *J. Alloys Compd.*, 2019, **781**, 820–830.

42 J. Yang, X. Zhang, G. Liu, L. Zhao, J. Liu, Z. Shi, J. Ding and G. Qiao, *Nano Energy*, 2020, **74**, 104826.

43 H. Wang, E. Schechtel, Y. Pei and G. J. Snyder, *Adv. Energy Mater.*, 2013, **3**, 488–495.

44 M. Li, Y. Liu, Y. Zhang, X. Han, K. Xiao, M. Nabahat, J. Arbiol, J. Llorca, M. Ibáñez and A. Cabot, *ACS Appl. Mater. Interfaces*, 2021, **13**, 51373–51382.

45 M. Ibáñez, Z. Luo, A. Genç, L. Piveteau, S. Ortega, D. Cadavid, O. Dobrozhan, Y. Liu, M. Nachtegaal, M. Zebarjadi, J. Arbiol, M. V. Kovalenko and A. Cabot, *Nat. Commun.*, 2016, **7**, 10766.

46 Y. Z. Pei, X. Y. Shi, A. LaLonde, H. Wang, L. D. Chen and G. J. Snyder, *Nature*, 2011, **473**, 66–69.

47 B. Jiang, X. Liu, Q. Wang, J. Cui, B. Jia, Y. Zhu, J. Feng, Y. Qiu, M. Gu, Z. Ge and J. He, *Energy Environ. Sci.*, 2020, **13**, 579–591.

48 R. J. Korkosz, T. C. Chasapis, S.-H. Lo, J. W. Doak, Y. J. Kim, C.-I. Wu, E. Hatzikraniotis, T. P. Hogan, D. N. Seidman, C. Wolverton, V. P. Dravid and M. G. Kanatzidis, *J. Am. Chem. Soc.*, 2014, **136**, 3225–3237.

49 S. A. Yamini, H. Wang, D. Ginting, D. R. Mitchell, S. X. Dou and G. J. Snyder, *ACS Appl. Mater. Interfaces*, 2014, **6**, 11476–11483.

50 D. Ginting, C.-C. Lin, L. Rathnam, J. H. Yun, B.-K. Yu, S.-J. Kim and J.-S. Rhyee, *J. Mater. Chem. A*, 2017, **5**, 13535–13543.

51 S. A. Yamini, H. Wang, Z. M. Gibbs, Y. Pei, S. X. Dou and G. J. Snyder, *Phys. Chem. Chem. Phys.*, 2014, **16**, 1835–1840.

52 D. Ginting, C.-C. Lin, R. Lydia, H. S. So, H. Lee, J. Hwang, W. Kim, R. Al Rahal Al Orabi and J.-S. Rhyee, *Acta Mater.*, 2017, **131**, 98–109.

53 H. J. Goldsmid, *Materials*, 2014, **7**, 2577–2592.

54 Y. Feutelais, B. Legendre, N. Rodier and V. Agafonov, *Mater. Res. Bull.*, 1993, **28**, 591–596.

55 A. Soni, Z. Yanyuan, Y. Ligen, M. K. K. Aik, M. S. Dresselhaus and Q. Xiong, *Nano Lett.*, 2012, **12**, 1203–1209.

56 C. Zhang, M. de la Mata, Z. Li, F. J. Belarre, J. Arbiol, K. A. Khor, D. Poletti, B. Zhu, Q. Yan and Q. Xiong, *Nano Energy*, 2016, **30**, 630–638.

57 N. K. Singh, J. Pandey, S. Acharya and A. Soni, *J. Alloys Compd.*, 2018, **746**, 350–355.

58 R. Pathak, P. Dutta, A. Srivastava, D. Rawat, R. K. Gopal, A. K. Singh, A. Soni and K. Biswas, *Angew. Chem., Int. Ed.*, 2022, **61**, e202210783.

59 J. R. Sootsman, D. Y. Chung and M. G. Kanatzidis, *Angew. Chem., Int. Ed.*, 2009, **48**, 8616–8639.

60 S. I. Kim, K. H. Lee, H. A. Mun, H. S. Kim, S. W. Hwang, J. W. Roh, D. J. Yang, W. H. Shin, X. S. Li, Y. H. Lee, G. J. Snyder and S. W. Kim, *Science*, 2015, **348**, 109–114.

61 Y. Pan, U. Aydemir, J. A. Grovogui, I. T. Witting, R. Hanus, Y. Xu, J. Wu, C.-F. Wu, F.-H. Sun, H.-L. Zhuang, J.-F. Dong, J.-F. Li, V. P. Dravid and G. J. Snyder, *Adv. Mater.*, 2018, **30**, 1802016.

62 M. Hong, T. C. Chasapis, Z.-G. Chen, L. Yang, M. G. Kanatzidis, G. J. Snyder and J. Zou, *ACS Nano*, 2016, **10**, 4719–4727.

63 A. M. Adam, E. Lilov and P. Petkov, *Superlattices Microstruct.*, 2017, **101**, 609–624.

64 R. Venkatasubramanian, E. Siivola, T. Colpitts and B. O'Quinn, *Nature*, 2001, **413**, 597–602.

65 V. A. Kulbachinskii, N. Miura, H. Arimoto, T. Ikaida, P. Lostak, H. Horak and C. Drasar, *J. Phys. Soc. Jpn.*, 1999, **68**, 3328–3333.

66 T. Kyratsi, E. Hatzikraniotis, K. M. Paraskevopoulos and K. Chrissafis, *Ionics*, 1997, **3**, 305–309.

67 J. Horák, Z. Stary, P. Lošťák and J. Pancíř, *J. Phys. Chem. Solids*, 1990, **51**, 1353–1360.

68 J. Horak, S. Karamazov and P. Lošťák, *Radiat. Eff. Defects Solids*, 1997, **140**, 181–196.

69 L.-D. Zhao, S.-H. Lo, Y. Zhang, H. Sun, G. Tan, C. Uher, C. Wolverton, V. P. Dravid and M. G. Kanatzidis, *Nature*, 2014, **508**, 373–377.

70 K. Peng, B. Zhang, H. Wu, H. Che, X. Sun, J. Ying, G. Wang, Z. Sun, G. Wang and X. Zhou, *J. Mater. Chem. C*, 2020, **8**, 9345–9351.

71 Q. Zhang, E. K. Chere, J. Sun, F. Cao, K. Dahal, S. Chen, G. Chen and Z. Ren, *Adv. Energy Mater.*, 2015, **5**, 1500360.

72 C. Chang, M. Wu, D. He, Y. Pei, C.-F. Wu, X. Wu, H. Yu, F. Zhu, K. Wang, Y. Chen, L. Huang, J.-F. Li, J. He and L.-D. Zhao, *Science*, 2018, **360**, 778–783.

73 L.-D. Zhao, G. Tan, S. Hao, J. He, Y. Pei, H. Chi, H. Wang, S. Gong, H. Xu, V. P. Dravid, C. Uher, G. J. Snyder, C. Wolverton and M. G. Kanatzidis, *Science*, 2016, **351**, 141–144.

74 L.-D. Zhao, C. Chang, G. Tan and M. G. Kanatzidis, *Energy Environ. Sci.*, 2016, **9**, 3044–3060.

75 B. Qin, D. Wang, X. Liu, Y. Qin, J.-F. Dong, J. Luo, J.-W. Li, W. Liu, G. Tan, X. Tang, J.-F. Li, J. He and L.-D. Zhao, *Science*, 2021, **373**, 556–561.

76 L. Su, D. Wang, S. Wang, B. Qin, Y. Wang, Y. Qin, Y. Jin, C. Chang and L.-D. Zhao, *Science*, 2022, **375**, 1385–1389.

77 G. Yang, L. Sang, M. Li, S. M. K. N. Islam, Z. Yue, L. Liu, J. Li, D. R. G. Mitchell, N. Ye and X. Wang, *ACS Appl. Mater. Interfaces*, 2020, **12**, 12910–12918.

78 T.-R. Wei, G. Tan, X. Zhang, C.-F. Wu, J.-F. Li, V. P. Dravid, G. J. Snyder and M. G. Kanatzidis, *J. Am. Chem. Soc.*, 2016, **138**, 8875–8882.

79 Y. Gong, C. Chang, W. Wei, J. Liu, W. Xiong, S. Chai, D. Li, J. Zhang and G. Tang, *Scr. Mater.*, 2018, **147**, 74–78.

80 Y. Fu, J. Xu, G.-Q. Liu, J. Yang, X. Tan, Z. Liu, H. Qin, H. Shao, H. Jiang and B. Liang, *J. Mater. Chem. C*, 2016, **4**, 1201–1207.

81 S. R. Popuri, M. Pollet, R. Decourt, F. D. Morrison, N. S. Bennett and J.-W. G. Bos, *J. Mater. Chem. C*, 2016, **4**, 1685–1691.

82 Q. Tan and J.-F. Li, *J. Electron. Mater.*, 2014, **43**, 2435–2439.

83 H. Wu, X. Lu, G. Wang, K. Peng, H. Chi, B. Zhang, Y. Chen, C. Li, Y. Yan, L. Guo, C. Uher, X. Zhou and X. Han, *Adv. Energy Mater.*, 2018, **8**, 1800087.

84 W. He, D. Wang, J.-F. Dong, Y. Qiu, L. Fu, Y. Feng, Y. Hao, G. Wang, J. Wang, C. Liu, J.-F. Li, J. He and L.-D. Zhao, *J. Mater. Chem. A*, 2018, **6**, 10048–10056.

85 W. He, D. Wang, H. Wu, Y. Xiao, Y. Zhang, D. He, Y. Feng, Y.-J. Hao, J.-F. Dong, R. Chetty, L. Hao, D. Chen, J. Qin, Q. Yang, X. Li, J.-M. Song, Y. Zhu, W. Xu, C. Niu, X. Li, G. Wang, C. Liu, M. Ohta, S. J. Pennycook, J. He, J.-F. Li and L.-D. Zhao, *Science*, 2019, **365**, 1418–1424.

86 Z. Zhou, J. Yang, Q. Jiang, X. Lin, J. Xin, A. Basit, J. Hou and B. Sun, *Nano Energy*, 2018, **47**, 81–88.

87 G. Tan, F. Shi, S. Hao, H. Chi, L.-D. Zhao, C. Uher, C. Wolverton, V. P. Dravid and M. G. Kanatzidis, *J. Am. Chem. Soc.*, 2015, **137**, 5100–5112.

88 G. Tan, F. Shi, J. W. Doak, H. Sun, L.-D. Zhao, P. Wang, C. Uher, C. Wolverton, V. P. Dravid and M. G. Kanatzidis, *Energy Environ. Sci.*, 2015, **8**, 267–277.

89 G. Tan, L.-D. Zhao, F. Shi, J. W. Doak, S.-H. Lo, H. Sun, C. Wolverton, V. P. Dravid, C. Uher and M. G. Kanatzidis, *J. Am. Chem. Soc.*, 2014, **136**, 7006–7017.

90 G. Tan, F. Shi, S. Hao, H. Chi, T. P. Bailey, L.-D. Zhao, C. Uher, C. Wolverton, V. P. Dravid and M. G. Kanatzidis, *J. Am. Chem. Soc.*, 2015, **137**, 11507–11516.

91 G. Tan, F. Shi, H. Sun, L.-D. Zhao, C. Uher, V. P. Dravid and M. G. Kanatzidis, *J. Mater. Chem. A*, 2014, **2**, 20849–20854.

92 Y. Wu, B. Zhou, L. Liu, S. Dai, L. Song and J. Yang, *Research*, 2025, **8**, 0727.

93 Z. Song, H. Liu, Z. Du, X. Liu and J. Cui, *Phys. Status Solidi A*, 2016, **213**, 986–993.

94 P. Wyżga, S. Grimm, V. Garbe, E. Zuñiga-Puelles, C. Himcinschi, I. Veremchuk, A. Leithe-Jasper and R. Gumeniuk, *J. Mater. Chem. C*, 2021, **9**, 4008–4019.

95 M. R. Shankar, A. N. Prabhu and T. Srivastava, *Mater. Adv.*, 2024, **5**, 9823–9837.

96 J. H. Jeon, D. H. Kim, S. Hong, W. H. Shin, N. V. Du, H.-S. Kim, T. Kim and S.-I. Kim, *Electron. Mater. Lett.*, 2021, **17**, 340–346.

97 J.-I. Kim, H.-S. Kim and S.-I. Kim, *J. Phys. D: Appl. Phys.*, 2019, **52**, 295501.

98 G. Dennler, R. Chmielowski, S. Jacob, F. Capet, P. Roussel, S. Zastrow, K. Nielsch, I. Opahle and G. K. H. Madsen, *Adv. Energy Mater.*, 2014, **4**, 1301581.

99 D. R. Brown, T. Day, T. Caillat and G. J. Snyder, *J. Electron. Mater.*, 2013, **42**, 2014–2019.

100 O. Mayasree, C. R. Sankar, K. M. Kleinke and H. Kleinke, *Coord. Chem. Rev.*, 2012, **256**, 1377–1383.

101 P. Qiu, M. T. Agne, Y. Liu, Y. Zhu, H. Chen, T. Mao, J. Yang, W. Zhang, S. M. Haile, W. G. Zeier, J. Janek, C. Uher, X. Shi, L. Chen and G. J. Snyder, *Nat. Commun.*, 2018, **9**, 2910.

102 P. Qiu, X. Shi and L. Chen, *Energy Storage Mater.*, 2016, **3**, 85–97.

103 T. Wei, Y. Qin, T. Deng, Q. Song, B. Jiang, R. Liu, P. Qiu, X. Shi and L. Chen, *Sci. China Mater.*, 2018, **62**, 1–17.

104 H. Liu, X. Shi, F. Xu, L. Zhang, W. Zhang, L. Chen, Q. Li, C. Uher, T. Day and G. J. Snyder, *Nat. Mater.*, 2012, **11**, 422–425.

105 Y. He, T. Day, T. Zhang, H. Liu, X. Shi, L. Chen and G. J. Snyder, *Adv. Mater.*, 2014, **26**, 3974–3978.

106 W. C. Pilgrim and C. Morkel, *J. Phys.: Condens. Matter*, 2006, **18**, R585–R633.

107 K. Trachenko, *Phys. Rev. B: Condens. Matter Mater. Phys.*, 2008, **78**, 104201.

108 M. K. Balapanov, I. G. Gafurov, U. K. Mukhamed'yanov, R. A. Yakshibaev and R. K. Ishembetov, *Phys. Status Solidi B*, 2004, **241**, 114–119.

109 Y. Zhang, C. Xing, Y. Liu, M. C. Spadaro, X. Wang, M. Li, K. Xiao, T. Zhang, P. Guardia, K. H. Lim, A. O. Moghaddam, J. Llorca, J. Arbiol, M. Ibáñez and A. Cabot, *Nano Energy*, 2021, **85**, 105991.

110 H. Luo, D. Yang, Y. Yu, Q. Liang, H. Peng, F. Xia, X. Tang and J. Wu, *Adv. Electron. Mater.*, 2022, **8**, 2100835.

111 Y. He, P. Lu, X. Shi, F. Xu, T. Zhang, G. J. Snyder, C. Uher and L. Chen, *Adv. Mater.*, 2015, **27**, 3639–3644.

112 G. Sorokin, Y. M. Papshev and P. Oush, *Sov. Phys. Solid State*, 1966, **7**, 1810–1811.

113 H. Liu, X. Yuan, P. Lu, X. Shi, F. Xu, Y. He, Y. Tang, S. Bai, W. Zhang, L. Chen, Y. Lin, L. Shi, H. Lin, X. Gao, X. Zhang, H. Chi and C. Uher, *Adv. Mater.*, 2013, **25**, 6607–6612.

114 B. Gahtori, S. Bathula, K. Tyagi, M. Jayasimhadri, A. K. Srivastava, S. Singh, R. C. Budhani and A. Dhar, *Nano Energy*, 2015, **13**, 36–46.

115 B. Yu, W. Liu, S. Chen, H. Wang, H. Wang, G. Chen and Z. Ren, *Nano Energy*, 2012, **1**, 472–478.

116 W.-D. Liu, L. Yang, Z.-G. Chen and J. Zou, *Adv. Mater.*, 2020, **32**, 1905703.

117 S. Rehman, K. Kim, J.-H. Hur and D.-K. Kim, *J. Phys. D: Appl. Phys.*, 2017, **50**, 135301.

118 H. T. J. Evans, *Am. Mineral.*, 1981, **66**, 807–818.

119 C. Coughlan, M. Ibáñez, O. Dobrozhan, A. Singh, A. Cabot and K. M. Ryan, *Chem. Rev.*, 2017, **117**, 5865–6109.

120 X. Su, F. Fu, Y. Yan, G. Zheng, T. Liang, Q. Zhang, X. Cheng, D. Yang, H. Chi, X. Tang, Q. Zhang and C. Uher, *Nat. Commun.*, 2014, **5**, 4908.

121 L.-L. Zhao, X.-L. Wang, J.-Y. Wang, Z.-X. Cheng, S.-X. Dou, J. Wang and L.-Q. Liu, *Sci. Rep.*, 2015, **5**, 7671.

122 A. A. Olvera, N. A. Moroz, P. Sahoo, P. Ren, T. P. Bailey, A. A. Page, C. Uher and P. F. P. Poudeu, *Energy Environ. Sci.*, 2017, **10**, 1668–1676.

123 P. Qiu, T. Mao, Z. Huang, X. Xia, J. Liao, M. T. Agne, M. Gu, Q. Zhang, D. Ren, S. Bai, X. Shi, G. J. Snyder and L. Chen, *Joule*, 2019, **3**, 1538–1548.

124 T. W. Day, K. S. Weldert, W. G. Zeier, B.-R. Chen, S. L. Moffitt, U. Weis, K. P. Jochum, M. Panthöfer, M. J. Bedzyk, G. J. Snyder and W. Tremel, *Chem. Mater.*, 2015, **27**, 7018–7027.

125 L. Zhao, X. Wang, F. Y. Fei, J. Wang, Z. Cheng, S. Dou, J. Wang and G. J. Snyder, *J. Mater. Chem. A*, 2015, **3**, 9432–9437.

126 K. Zhao, A. B. Blichfeld, H. Chen, Q. Song, T. Zhang, C. Zhu, D. Ren, R. Hanus, P. Qiu, B. B. Iversen, F. Xu, G. J. Snyder, X. Shi and L. Chen, *Chem. Mater.*, 2017, **29**, 6367–6377.

127 K. Zhao, A. B. Blichfeld, E. Eikeland, P. Qiu, D. Ren, B. B. Iversen, X. Shi and L. Chen, *J. Mater. Chem. A*, 2017, **5**, 18148–18156.

128 K. Zhao, P. Qiu, Q. Song, A. B. Blichfeld, E. Eikeland, D. Ren, B. Ge, B. B. Iversen, X. Shi and L. Chen, *Mater. Today Phys.*, 2017, **1**, 14–23.

129 S. Ballikaya, H. Chi, J. R. Salvador and C. Uher, *J. Mater. Chem. A*, 2013, **1**, 12478–12484.

130 D. R. Brown, T. Day, K. A. Borup, S. Christensen, B. B. Iversen and G. J. Snyder, *APL Mater.*, 2013, **1**, 052107.

131 S. Yang, L. Li, C. Lin, J. Wan, Y. Lin and M. Luo, *Sci. Adv.*, 2025, **11**, eadz7487.

132 S. Bhattacharya, R. Basu, R. Bhatt, S. Pitale, A. Singh, D. K. Aswal, S. K. Gupta, M. Navaneethan and Y. Hayakawa, *J. Mater. Chem. A*, 2013, **1**, 11289–11294.

133 D. Srivastava, G. C. Tewari and M. Karppinen, *J. Phys.: Condens. Matter*, 2014, **26**, 505501.

134 F. M. R. Engelsman, G. A. Wiegers, F. Jellinek and B. Van Laar, *J. Solid State Chem.*, 1973, **6**, 574–582.

135 G. C. Tewari, T. S. Tripathi and A. K. Rastogi, *Z. Kristallogr.*, 2010, **225**, 471–474.

136 G. C. Tewari, T. S. Tripathi, P. Kumar, A. K. Rastogi, S. K. Pasha and G. Gupta, *J. Electron. Mater.*, 2011, **40**, 2368–2373.

137 G. C. Tewari, T. S. Tripathi, H. Yamauchi and M. Karppinen, *Mater. Chem. Phys.*, 2014, **145**, 156–161.

138 D. Srivastava, G. C. Tewari, M. Karppinen and R. M. Nieminen, *J. Phys.: Condens. Matter*, 2013, **25**, 105504.

139 R. Yano and T. Sasagawa, *Cryst. Growth Des.*, 2016, **16**, 5618–5623.

140 K. S. Rana, A. Singh, A. Bhui, K. Biswas and A. Soni, *ACS Appl. Energy Mater.*, 2024, **7**, 5621–5628.

141 A. Gagor, D. Gnida and A. Pietraszko, *Mater. Chem. Phys.*, 2014, **146**, 283–288.

142 J. L. Niedziela, D. Bansal, A. F. May, J. Ding, T. Lanigan-Atkins, G. Ehlers, D. L. Abernathy, A. Said and O. Delaire, *Nat. Phys.*, 2018, **15**, 73–78.

143 A. Basit, J. Xin, G. Murtaza, L. Wei, A. Hameed, W. Guoyu and J. Y. Dai, *EcoMat*, 2023, **5**, e12391.

144 G. C. Tewari, M. Karppinen and A. K. Rastogi, *J. Solid State Chem.*, 2013, **198**, 108–113.

145 A. I. Romanenko, G. E. Chebanova, I. N. Katamanin, M. V. Drozhzhin, S. B. Artemkina, M. K. Han, S. J. Kim and H. Wang, *J. Phys. D: Appl. Phys.*, 2022, **55**, 135302.

146 Y. Li, Z. Dong, Z. Li, Y. Zhang, K. Guo, J. Xing, J. Zhang and J. Luo, *Mater. Today Phys.*, 2023, **31**, 100995.

147 G. C. Tewari, T. S. Tripathi and A. K. Rastogi, *J. Electron. Mater.*, 2010, **39**, 1133–1139.

148 A. Kaltzoglou, P. Vaqueiro, T. Barbier, E. Guilmeau and A. V. Powell, *J. Electron. Mater.*, 2014, **43**, 2029–2034.

149 E. Shkvarina, A. Shkvarin, A. Titov, M. Postnikov, J. Plaisier, L. Gigli, M. Gaboardi and A. Titov, *J. Solid State Chem.*, 2024, **330**, 124497.

150 Y. Cheng, J. Yang, Q. Jiang, L. Fu, Y. Xiao, Y. Luo, D. Zhang and M. Zhang, *J. Am. Ceram. Soc.*, 2015, **98**, 3975–3980.

151 Y. Yan, L. Guo, Z. Zhang, X. Lu, K. Peng, W. Yao, J. Dai, G. Wang and X. Zhou, *Scr. Mater.*, 2017, **127**, 127–131.

152 H. S. Kousar, D. Srivastava, M. Karppinen and G. C. Tewari, *Z. Anorg. Allg. Chem.*, 2023, **649**, e202300079.

153 G. C. Tewari, H. S. Kousar, D. Srivastava and M. Karppinen, *J. Magn. Magn. Mater.*, 2024, **590**, 171688.

154 L.-D. Zhao, J. He, D. Berardan, Y. Lin, J.-F. Li, C.-W. Nan and N. Dragoe, *Energy Environ. Sci.*, 2014, **7**, 2900–2924.

155 J. Li, J. Sui, Y. Pei, C. Barreteau, D. Berardan, N. Dragoe, W. Cai, J. He and L.-D. Zhao, *Energy Environ. Sci.*, 2012, **5**, 8543–8547.

156 F. Li, T.-R. Wei, F. Kang and J.-F. Li, *J. Mater. Chem. A*, 2013, **1**, 11942–11949.

157 J.-L. Lan, Y.-C. Liu, B. Zhan, Y.-H. Lin, B. Zhang, X. Yuan, W. Zhang, W. Xu and C.-W. Nan, *Adv. Mater.*, 2013, **25**, 5086–5090.

158 Y. Liu, J. Lan, W. Xu, Y. Liu, Y.-L. Pei, B. Cheng, D.-B. Liu, Y.-H. Lin and L.-D. Zhao, *Chem. Commun.*, 2013, **49**, 8075–8077.

159 S. Schwarzmüller, D. Souchay, D. Günther, A. Gocke, I. Dovgaliuk, S. Miller, G. Snyder and O. Oeckler, *Z. Anorg. Allg. Chem.*, 2018, **644**, 1915–1922.

160 S. Xu, Y. Zhu, W. Guo, P. Han, S. Lou, H. Ming, Y. Zheng, Z.-Z. Luo and Z. Zou, *Adv. Energy Mater.*, 2026, **16**, e05461.

161 F. Reissig, B. Heep, M. Panthöfer, M. Wood, S. Anand, G. J. Snyder and W. Tremel, *Dalton Trans.*, 2019, **48**, 15822–15829.

162 Y.-F. Tsai, C. L. Stern, B.-C. Chen, G. J. Snyder and H.-J. Wu, *J. Mater. Chem. A*, 2023, **11**, 10532–10537.

163 O. Cherniushok, T. Parashchuk, J. Tobola, S. D. N. Luu, A. Pogodin, O. Kokhan, I. Studenyak, I. Barchiy, M. Piasecki and K. T. Wojciechowski, *ACS Appl. Mater. Interfaces*, 2021, **13**, 39606–39620.

164 T. Parashchuk, O. Cherniushok, B. Wiendlocha, J. Tobola, R. Cardoso-Gil, G. J. Snyder, Y. Grin and K. T. Wojciechowski, *Adv. Funct. Mater.*, 2025, **35**, 2502163.

165 Y. Zhang, E. Skoug, J. Cain, V. Ozoliņš, D. Morelli and C. Wolverton, *Phys. Rev. B: Condens. Matter Mater. Phys.*, 2012, **85**, 054306.

166 T.-R. Wei, F. Li and J.-F. Li, *J. Electron. Mater.*, 2014, **43**, 2229–2238.

167 T. Plirdpring, K. Kurosaki, A. Kosuga, T. Day, S. Firdosy, V. Ravi, G. J. Snyder, A. Harnwunggmoung, T. Sugahara, Y. Ohishi, H. Muta and S. Yamanaka, *Adv. Mater.*, 2012, **24**, 3622–3626.

168 R. Liu, L. Xi, H. Liu, X. Shi, W. Zhang and L. Chen, *Chem. Commun.*, 2012, **48**, 3818–3820.

169 Y. Luo, J. Yang, Q. Jiang, W. Li, D. Zhang, Z. Zhou, Y. Cheng, Y. Ren and X. He, *Adv. Energy Mater.*, 2016, **6**, 1600007.

170 X. Shi, L. Xi, J. Fan, W. Zhang and L. Chen, *Chem. Mater.*, 2010, **22**, 6029–6031.

171 X. Shi, F. Huang, M. Liu and L. Chen, *Appl. Phys. Lett.*, 2009, **94**, 122103.

172 P. Vaqueiro, G. Guélou, A. Kaltzoglou, R. I. Smith, T. Barbier, E. Guilmeau and A. V. Powell, *Chem. Mater.*, 2017, **29**, 4080–4090.

173 J. Heo, G. Laurita, S. Muir, M. A. Subramanian and D. A. Keszler, *Chem. Mater.*, 2014, **26**, 2047–2051.

174 Y. Bouyrie, M. Ohta, K. Suekuni, Y. Kikuchi, P. Jood, A. Yamamoto and T. Takabatake, *J. Mater. Chem. C*, 2017, **5**, 4174–4184.

175 P. Qiu, T. Zhang, Y. Qiu, X. Shi and L. Chen, *Energy Environ. Sci.*, 2014, **7**, 4000–4006.

176 L. Xi, Y. B. Zhang, X. Y. Shi, J. Yang, X. Shi, L. D. Chen, W. Zhang, J. Yang and D. J. Singh, *Phys. Rev. B: Condens. Matter Mater. Phys.*, 2012, **86**, 155201.

177 M.-L. Liu, F.-Q. Huang, L.-D. Chen and I.-W. Chen, *Appl. Phys. Lett.*, 2009, **94**, 202103.

178 M.-L. Liu, I.-W. Chen, F.-Q. Huang and L.-D. Chen, *Adv. Mater.*, 2009, **21**, 3808–3812.

179 C. Rincón, *Solid State Commun.*, 1987, **64**, 663–665.

180 S.-H. Wei, L. G. Ferreira and A. Zunger, *Phys. Rev. B: Condens. Matter Mater. Phys.*, 1992, **45**, 2533–2536.

181 H. Wu and Z. Dong, *Acta Mater.*, 2016, **118**, 331–341.

182 K. Yu and E. A. Carter, *Chem. Mater.*, 2016, **28**, 864–869.

183 S. Schorr and G. Gonzalez-Aviles, *Phys. Status Solidi A*, 2009, **206**, 1054–1058.

184 J. Fan, W. Carrillo-Cabrera, L. Akselrud, I. Antonyshyn, L. Chen and Y. Grin, *Inorg. Chem.*, 2013, **52**, 11067–11074.

185 D. Zhang, G. Fu and S. Wang, in *Novel Thermoelectric Materials and Device Design Concepts*, ed. S. Skipidarov and M. Nikitin, Springer International Publishing, Cham, 2019, pp. 137–157. DOI: 10.1007/978-3-030-12057-3_7.

186 X. Yuan, Y. Zhao, P. Sui, J. Ni and Z. Dai, *J. Mater. Chem. A*, 2025, **13**, 5106–5118.

187 F. Li, X. Liu, N. Ma, Y.-C. Yang, J.-P. Yin, L. Chen and L.-M. Wu, *J. Am. Chem. Soc.*, 2023, **145**, 14981–14993.

188 N. N. Patil, R. Wu, C. Fiedler, N. Kapuria, B. Nan, N. Jakhar, A. Cabot, M. Ibáñez, K. M. Ryan, A. M. Ganose and S. Singh, *ACS Energy Lett.*, 2026, **11**, 481–488.

189 M. M. Kubenova, K. A. Kuterbekov, M. K. Balapanov, R. K. Ishembetov, A. M. Kabyshev and K. Z. Bekmyrza, *Nanomaterials*, 2021, **11**, 2238.

190 Y. Wang, H. Zhao, S. Shahabfar, T. S. Ie, S. Sasmal, S. Rosenkranz, C. Wolverton, D. Y. Chung and M. G. Kanatzidis, *Inorg. Chem.*, 2025, **64**, 20977–20985.

191 C. C. Laing, J. Shen, M. A. Quintero, B. E. Weiss, Y. Xia, Z. Li, J. He, C. Wolverton and M. G. Kanatzidis, *Chem. Mater.*, 2022, **34**, 3409–3422.

192 J. M. Hodges, Y. Xia, C. D. Malliakas, T. J. Slade, C. Wolverton and M. G. Kanatzidis, *Chem. Mater.*, 2020, **32**, 10146–10154.

193 P. Jafarzadeh, M. R. Rodrigues, Y. Shi, A. Assoud, T. Zou, J. B. Kycia and H. Kleinke, *Dalton Trans.*, 2019, **48**, 9357.

194 F. Q. Huang and J. A. Ibers, *Inorg. Chem.*, 1999, **38**, 5978–5983.

195 O. Cherniushok, O. V. Smitiukh, D. Wieczorek, O. V. Marchuk, B. Wiendlocha, T. Parashchuk and K. T. Wojciechowski, *Chem. Mater.*, 2025, **37**, 7377–7389.

196 S. Fei, M. Miyata, M. Takahashi, P. Dwivedi, W. Zhou, M. Ohta and S. Maenosono, *AIP Adv.*, 2020, **10**, 075021.

197 L. J. Cabri, D. C. Harris and J. M. Stewart, *Can. Mineral.*, 1970, **10**, 232–246.

198 L. J. Cabri, D. C. Harris and J. M. Stewart, *Am. Mineral.*, 1970, **55**, 10–17.

199 R. Henry, J. Steger, H. Nahigian and A. Wold, *Inorg. Chem.*, 1975, **14**, 2915–2917.

200 J. F. Rowland, E. J. Gabe and S. R. Hall, *Can. Mineral.*, 1975, **13**, 188–196.

201 R. Chmielowski, S. Bhattacharya, S. Jacob, D. Péré, A. Jacob, K. Moriya, B. Delatouche, P. Roussel, G. Madsen and G. Dennler, *Sci. Rep.*, 2017, **7**, 46630.

202 M. R. Allazov and Z. T. Gulieva, *Zh. Neorg. Khim.*, 1988, **33**, 1887–1891.

203 R. Carlini, C. Artini, G. Borzone, R. Masini, G. Zanicchi and G. A. Costa, *J. Therm. Anal. Calorim.*, 2010, **103**, 23–27.

204 Q. Du, M. Abeykoon, Y. Liu, G. Kotliar and C. Petrovic, *Phys. Rev. Lett.*, 2019, **123**, 076602.

205 S. Bhattacharya, R. Chmielowski, G. Dennler and G. K. H. Madsen, *J. Mater. Chem. A*, 2016, **4**, 11086–11093.

206 Z. Liu, H. Geng, J. Shuai, Z. Wang, J. Mao, D. Wang, Q. Jie, W. Cai, J. Sui and Z. Ren, *J. Mater. Chem. C*, 2015, **3**, 10442–10450.

207 O. A. Moghaddam, A. Shokuhfar and A. Cabot, *Iran. J. Mater. Sci. Eng.*, 2019, **16**, 20–26.

208 W. Gao, Y. Yang, M. Deng, B. Sun, Y. Fu, X. Wei, Y. Li, Z. Liu and J. Sui, *J. Mater. Chem. A*, 2022, **10**, 19829–19838.

209 R. Chmielowski, S. Bhattacharya, W. Xie, D. Péré, S. Jacob, R. Stern, K. Moriya, A. Weidenkaff, G. K. H. Madsen and G. Dennler, *J. Mater. Chem. C*, 2016, **4**, 3094–3100.

210 G. Guélou, F. Failamani, P. Sauerschnig, J. Waybright, K. Suzuta and T. Mori, *J. Mater. Chem. C*, 2020, **8**, 1811–1818.

211 W. Yao, D. Yang, Y. Yan, K. Peng, H. Zhan, A. Liu, X. Lu, G. Wang and X. Zhou, *ACS Appl. Mater. Interfaces*, 2017, **9**, 10595–10601.

212 N. Prasad and B. Karthikeyan, *J. Appl. Phys.*, 2019, **125**, 085702.

213 D. G. Cahill, S. K. Watson and R. O. Pohl, *Phys. Rev. B: Condens. Matter Mater. Phys.*, 1992, **46**, 6131–6140.

214 D. Parker, A. F. May, H. Wang, M. A. McGuire, B. C. Sales and D. J. Singh, *Phys. Rev. B: Condens. Matter Mater. Phys.*, 2013, **87**, 045205.

215 D. Yang, Y. Tang, H. Yang, W. Li, B. Zhang, W. Yao, G. Wang and X. Zhou, *J. Solid State Chem.*, 2022, **314**, 123342.

216 Y. You, X. Su, W. Liu, Y. Yan, T. Hu, C. Uher and X. Tang, *RSC Adv.*, 2017, **7**, 34466–34472.

217 W. Huang, H. Zhu, Q. Liu, S. Duan, M. Yang, X. Liu and T. Su, *J. Alloys Compd.*, 2024, **970**, 172555.

218 W. Huang, H. Zhu, Q. Liu, X. Zhou, S. Li, M. Hu and T. Su, *Solid State Sci.*, 2023, **135**, 107078.

219 Y. You, X. Su, W. Liu, Y. Yan, J. Fu, X. Cheng, C. Zhang and X. Tang, *J. Solid State Chem.*, 2018, **262**, 1–7.

220 H. S. Kousar, D. Srivastava, A. J. Karttunen, M. Karppinen and G. C. Tewari, *J. Mater. Chem. A*, 2024, **12**, 32338–32348.

221 P. Kaur and C. Bera, *Phys. Chem. Chem. Phys.*, 2017, **19**, 24928–24933.

222 J. Yang, D. Yang, Y. Wang, X. Quan and Y. Li, *J. Solid State Chem.*, 2021, **302**, 122443.

223 Y. You, X. Su, S. Hao, W. Liu, Y. Yan, T. Zhang, M. Zhang, C. Wolverton, M. G. Kanatzidis and X. Tang, *J. Mater. Chem. A*, 2018, **6**, 15123–15131.

224 H. S. Kousar, D. Srivastava, A. J. Karttunen, M. Karppinen and G. C. Tewari, *APL Mater.*, 2022, **10**, 091104.

225 S.-S. Zhang, D.-F. Yang, N. Shaheen, X.-C. Shen, D.-D. Xie, Y.-C. Yan, X. Lu and X.-Y. Zhou, *Rare Met.*, 2017, **37**, 326–332.

226 H. Nahigian, J. Steger, H. L. McKinzie, R. J. Arnott and A. Wold, *Inorg. Chem.*, 1974, **13**, 1498–1503.

227 H. S. Kousar, D. Srivastava, M. Karppinen and G. C. Tewari, *J. Phys.: Condens. Matter*, 2019, **31**, 405704.

228 G. Yamaguchi, M. Shimada and M. Koizumi, *J. Solid State Chem.*, 1976, **9**, 63–65.

229 P. Yadav, N. Dhariwal, A. Sanger, S. B. Kang and V. Kumar, *Nano Energy*, 2025, **135**, 110696.

230 X.-L. Shi, L. Wang, W. Lyu, T. Cao, W. Chen, B. Hu and Z.-G. Chen, *Chem. Soc. Rev.*, 2024, **53**, 9254–9305.

231 Y. Wang, P. Lin, Q. Lou, Z. Zhang, S. Huang, Y. Lu and J. He, *Mater. Adv.*, 2021, **2**, 2584–2593.

232 Y. Deng, M. Wei, Y. Lei, J. Lu, P. Peng, Y. Zhang and Z. Zheng, *CrystEngComm*, 2025, **27**, 1055–1077.

233 T.-R. Wei, P. Qiu, K. Zhao, X. Shi and L. Chen, *Adv. Mater.*, 2023, **35**, 2110236.

234 M. Zhu, X.-L. Shi, H. Wu, Q. Liu and Z.-G. Chen, *Chem. Eng. J.*, 2023, **473**, 145236.

235 H. Wu, X.-L. Shi, J. Duan, Q. Liu and Z.-G. Chen, *Energy Environ. Sci.*, 2023, **16**, 1870–1906.

236 S. Y. Tee, D. Ponsford, C. L. Lay, X. Wang, X. Wang, D. C. J. Neo, T. Wu, W. Thitsartarn, J. C. C. Yeo, G. Guan, T.-C. Lee and M.-Y. Han, *Adv. Sci.*, 2022, **9**, 2204624.

237 G. Li, Q. An, S. I. Morozov, B. Duan, W. A. Goddard III, Q. Zhang, P. Zhai and G. J. Snyder, *npj Comput. Mater.*, 2018, **4**, 44.

238 R. Zamiri, H. A. Ahangar, A. Zakaria, G. Zamiri, M. Shabani, B. Singh and J. M. F. Ferreira, *Chem. Cent. J.*, 2015, **9**, 28.

239 Y. Chang, Z. Li, P. Luo, W. Qian, J. Zhang and J. Luo, *Adv. Funct. Mater.*, 2024, **34**, 2310016.

240 D. Gao, S. Wang, Y. Wen, F. Fang, Y. Li, S. Liu, Y. Wang, H. Xie, Y. Qiu and L.-D. Zhao, *Mater. Today Phys.*, 2024, **41**, 101353.

241 P. Jood and M. Ohta, *ACS Appl. Energy Mater.*, 2020, **3**, 2160–2167.

242 K. Yu, Y. Wu, H. He, C. Niu, M. Rong, D. Wu, S. Liu and Y. Zhang, *J. Alloys Compd.*, 2021, **885**, 161378.

243 C. M. Fang, R. A. de Groot and G. A. Wiegers, *J. Phys. Chem. Solids*, 2002, **63**, 457–464.

244 Y. Pei, N. A. Heinz and G. J. Snyder, *J. Mater. Chem.*, 2011, **21**, 18256–18260.

245 M. Ferhat and J. Nagao, *J. Appl. Phys.*, 2000, **88**, 813–816.

246 A. K. Gautam and N. Khare, *J. Materiomics*, 2023, **9**, 310–317.

247 H. N. Nam, R. Yamada, H. Okumura, T. Q. Nguyen, K. Suzuki, H. Shinya, A. Masago, T. Fukushima and K. Sato, *Phys. Chem. Chem. Phys.*, 2021, **23**, 9773–9784.

248 H. Wuliji, K. Zhao, H. Jing, R. Ouyang, Y. Yang, T.-R. Wei, H. Zhu and X. Shi, *J. Materiomics*, 2024, **10**, 1270–1278.

249 H. N. Nam, K. Suzuki, A. Masago, T. Q. Nguyen, H. Shinya, T. Fukushima and K. Sato, *Appl. Phys. Lett.*, 2022, **120**, 143903.

250 K. Sato, S. Singh, I. Yamazaki, K. Hirata, A. K. R. Ang, M. Matsunami and T. Takeuchi, *AIP Adv.*, 2023, **13**, 125206.

251 K. Hirata, S. Singh and T. Takeuchi, *AIP Adv.*, 2023, **13**, 035122.

252 L. Li, C. Peng, J. Chen, Z. Ma, Y. Chen, S. Li, J. Wang and C. Wang, *J. Alloys Compd.*, 2021, **886**, 161241.

253 H. Wu, X.-L. Shi, Y. Mao, M. Li, T. Wu, D.-Z. Wang, L.-C. Yin, M. Zhu, W.-D. Liu, L. Wang, Y. Wang, J. Duan, Q. Liu and Z.-G. Chen, *Adv. Sci.*, 2024, **11**, 2408374.

254 K. Zhao, C. Zhu, W. Qiu, S. Yang, H. Su, P. Qiu, Y. He, M. Guan, T.-R. Wei, J. Ma, J. Liu, G. Zheng, F. Xu, X. Shi, J. He and L. Chen, *Matter*, 2022, **5**, 605–615.

255 Y. Wang, Q. Chen, P. Qiu, Z. Gao, S. Yang, L. Xi, J. Yang and X. Shi, *Adv. Funct. Mater.*, 2025, **35**, 2415008.

256 Z. Li, J. Zhang, P. Luo, J. Chen, B. Huang, Y. Sun and J. Luo, *ACS Appl. Mater. Interfaces*, 2023, **15**, 33605–33611.

257 L. Peng, S. Yang, T.-R. Wei, P. Qiu, J. Yang, Z. Zhang, X. Shi and L. Chen, *J. Materiomics*, 2022, **8**, 656–661.

258 S. Zhong, H. Luo, K. Liu, S. Chen, Z. Yang, Y. Zhong, J. Wu, X. Su, P. F. P. Poudeu, Q. Zhang and X. Tang, *ACS Appl. Mater. Interfaces*, 2024, **16**, 36637–36648.

259 M. Jin, X. Lu, L. Guo, F. He, X. Bai, R. Li and S. Lin, *Solid State Commun.*, 2023, **364**, 115123.

260 J. Liang, P. Qiu, Y. Zhu, H. Huang, Z. Gao, Z. Zhang, X. Shi and L. Chen, *Research*, 2020, **2020**, 6591981.

261 P. Jood, R. Chetty and M. Ohta, *J. Mater. Chem. A*, 2020, **8**, 13024–13037.

262 B. Nan, M. Li, Y. Zhang, K. Xiao, K. H. Lim, C. Chang, X. Han, Y. Zuo, J. Li, J. Arbiol, J. Llorca, M. Ibáñez and A. Cabot, *ACS Appl. Electron. Mater.*, 2024, **6**, 2807–2815.

263 J. Chen, H. Yuan, Y.-K. Zhu, K. Zheng, Z.-H. Ge, J. Tang, D. Zhou, L. Yang and Z.-G. Chen, *Inorg. Chem.*, 2021, **60**, 14165–14173.

264 Z. Li, J. Zhang, S. Wang, Z. Dong, C. Lin and J. Luo, *Scr. Mater.*, 2023, **228**, 115313.

265 S. Zhong, H. Bai, H. Luo, Q. Liang, K. Liu, Z. Yang, S. Chen, Q. Zhang, J. Wu, X. Su and X. Tang, *ACS Appl. Mater. Interfaces*, 2024, **16**, 1148–1157.

266 G. Li, Q. An, B. Duan, L. Borgsmiller, M. Al Malki, M. Agne, U. Aydemir, P. Zhai, Q. Zhang, S. I. Morozov, W. A. Goddard III and G. J. Snyder, *Mater. Sci. Eng., R*, 2021, **144**, 100607.

267 Y. Wang, P. Qiu, S. Yang, Z. Gao, L. Chen and X. Shi, *J. Materiomics*, 2024, **10**, 543–551.

268 H. Hu, Y. Wang, C. Fu, X. Zhao and T. Zhu, *Innovation*, 2022, **3**, 100341.

269 Y. Wang, A. Li, H. Hu, C. Fu and T. Zhu, *Adv. Funct. Mater.*, 2023, **33**, 2300189.

270 S. He, Y. Li, L. Liu, Y. Jiang, J. Feng, W. Zhu, J. Zhang, Z. Dong, Y. Deng, J. Luo, W. Zhang and G. Chen, *Sci. Adv.*, 2020, **6**, eaaz8423.

271 Z. Ji, Z. Li, L. Liu, Y. Zou, C.-A. Di and D. Zhu, *Adv. Mater. Technol.*, 2024, **9**, 2302128.

272 M. Zhu, X.-L. Shi, M. Li, H. Wu, D.-Z. Wang, L.-C. Yin, T. Wu, W.-D. Liu, Y. Huang, Z.-G. Chen and Q. Liu, *Mater. Horiz.*, 2025, **12**, 2380–2388.

273 R. Moshwan, X.-L. Shi, W.-D. Liu, J. Liu and Z.-G. Chen, *Nano Today*, 2024, **58**, 102475.

274 N. Oueldna, N. Sabi, H. Aziam, V. Trabadelo and H. Ben Youcef, *Mater. Horiz.*, 2024, **11**, 2323–2354.

275 R. K. Biswas and S. K. Pati, *Phys. Chem. Chem. Phys.*, 2024, **26**, 9340–9349.

276 H. Chen, C. Shao, S. Huang, Z. Gao, H. Huang, Z. Pan, K. Zhao, P. Qiu, T.-R. Wei and X. Shi, *Adv. Energy Mater.*, 2024, **14**, 2303473.

277 D. Xie, Y. Chang, T. Liu, Z. Li and J. Luo, *ACS Appl. Energy Mater.*, 2022, **5**, 8878–8884.

278 H. Wu, X.-L. Shi, Y. Mao, M. Li, W.-D. Liu, D.-Z. Wang, L.-C. Yin, M. Zhu, Y. Wang, J. Duan, Q. Liu and Z.-G. Chen, *Adv. Energy Mater.*, 2023, **13**, 2302551.

279 W. Ding, X. Shen, Z. Li, Z. Fan, Z. Chen, J. Chen, J. Luo, W. Li and Y. Pei, *ACS Energy Lett.*, 2024, **9**, 5483–5491.

280 Z. Fan, W. Ding, X. Shen, J. Luo, W. Li and Y. Pei, *Adv. Electron. Mater.*, 2025, **11**, 2400728.

281 L. Feng, A. Guo, K. Liu, H. Bai, J. Lv, Q. Zhang, J. Wu, X. Su, X. Tang and C. Uher, *Mater. Today Phys.*, 2023, **33**, 101051.

282 Y. Wang, A. Li, Y. Hong, T. Deng, P. Deng, Y. Huang, K. Liu, J. Wang, C. Fu and T. Zhu, *Nat. Mater.*, 2025, **24**, 1545–1553.

283 K. R. Ang, I. Yamazaki, K. Hirata, S. Singh, M. Matsunami and T. Takeuchi, *ACS Appl. Mater. Interfaces*, 2023, **15**, 46962–46970.

284 M. Wu, J. Li, Y. Liu, Z. Wang, P. Wei, W. Zhao and K. Cai, *ACS Appl. Mater. Interfaces*, 2023, **15**, 8415–8423.

285 Y. Fu, S. Kang, H. Gu, L. Tan, C. Gao, Z. Fang, S. Dai and C. Lin, *Adv. Sci.*, 2023, **10**, 2207642.

286 J. Vinodhini, S. Harish, H. Ikeda and M. Navaneethan, *Surf. Interfaces*, 2024, **54**, 105105.

287 S. Yang, Z. Gao, P. Qiu, J. Liang, T.-R. Wei, T. Deng, J. Xiao, X. Shi and L. Chen, *Adv. Mater.*, 2021, **33**, 2007681.

288 J. Liang, X. Zhang and C. Wan, *ACS Appl. Mater. Interfaces*, 2022, **14**, 52017–52024.

289 J. Zhou, X. Chen, Y. Zhang, M. Avdeev, J. Zhang and X. Shi, *Adv. Funct. Mater.*, 2026, **36**, e15882.

290 X. Shen, C.-C. Yang, Y. Liu, G. Wang, H. Tan, Y.-H. Tung, G. Wang, X. Lu, J. He and X. Zhou, *ACS Appl. Mater. Interfaces*, 2019, **11**, 2168–2176.

291 B. K. Heep, K. S. Weldert, Y. Krysiak, T. W. Day, W. G. Zeier, U. Kolb, G. J. Snyder and W. Tremel, *Chem. Mater.*, 2017, **29**, 4833–4839.

292 G. Tan, S. Hao, J. Zhao, C. Wolverton and M. G. Kanatzidis, *J. Am. Chem. Soc.*, 2017, **139**, 6467–6473.

293 Z. Liu, P. Luo, C. Liao, C. Xie, M. Ye, W. Xu, Z. Liu, J. Mei, G. Ding, Q. Zhang, X. Tang and G. Tan, *Adv. Energy Mater.*, 2026, **16**, e70729.

294 C. Xie, R. Li, W. Xu, B. Jin, X.-L. Shi, X. Tang, G. Tan and Z.-G. Chen, *Adv. Funct. Mater.*, 2025, **35**, 2421545.

295 Y. Yang, L. Yuan, Z. Chen, W. Guo, Y. Zheng, H. Ming, N. Zhuang, Z.-Z. Luo and Z. Zou, *Adv. Funct. Mater.*, 2025, **35**, 2501431.

296 K. Zhao, M. Li, H. Wuliji, H. Gao, H. Chen, P. Qiu, Z. Zhou and X. Shi, *Adv. Sci.*, 2025, **12**, e14105.

297 X. Shen, Y. Xia, C.-C. Yang, Z. Zhang, S. Li, Y.-H. Tung, A. Benton, X. Zhang, X. Lu, G. Wang, J. He and X. Zhou, *Adv. Funct. Mater.*, 2020, **30**, 2000526.

298 Y. Wu, X. Su, D. Yang, Q. Zhang and X. Tang, *ACS Appl. Mater. Interfaces*, 2021, **13**, 4185–4191.